UNIVERSITY OF CALIFORNIA
RIVERSIDE

Red Cell-Derived Fluorescence Contrast Agents for Biomedical Imaging

A Dissertation submitted in partial satisfaction
of the requirements for the degree of

Doctor of Philosophy

in

Bioengineering

by

Jack Tang

December 2019

Dissertation Committee:
Dr. Bahman Anvari, Chairperson
Dr. Joshua Morgan
Dr. Meera Nair
Dr. Valentine I. Vullev

The Dissertation of Jack Tang is approved:

_____

_____

_____

_____

Committee Chairperson

University of California, Riverside

Acknowledgements

Mom, for nurturing me when I needed it.

Dad, for being stern with me when I needed it. Also, for teaching 象棋 and 道德经.

My students, who have unknowingly taught me so much.

Previous graduate students: Yadir Guerrero, Baharak Bahmani, Mohammad Sarshar, Jill Larsen, and Vicente Nuñez for their attentive mentorship.

Current members of Anvari lab, for learning and striving with me: Thompson Lu, Raviraj Vankayala, Jenny Mac, Taylor Hanley, Joshua Burns, and Chi Hua Lee.

Sensei Kevin Bash for his attention, guidance, and for not breaking my hand.

Sensei Steve Rockett for his kindness, terrible jokes, and for his and Margaret Nambiar's support in teaching aikido to children with developmental disabilities.

Sensei Dr. Val Vullev for calling me a wimp and opening my mind a little. Also, for imparting some understanding of fluorescence and spectroscopy.

Sensei Tadashi Hiraoka, the Nakama family, JP, Brian Money, Phil Queller, Carson Sheckler, and rest of the Riverside Judo Club for their warmth, strength, and spirit.

Dr. Nate Gabor for his kind and humble greetings.

Dr. Perry Link for promoting academic excellence as an outstanding teacher.

Dr. Will Grover for his unrestrained enthusiasm for all things science.

Dr. Joshua Morgan for being an approachable and skilled role model.

Dr. B. Hyle Park for his continued service in the Department of Bioengineering.

Drs. Meera Nair and Jiang Li for their mentorship and support with flow cytometry.

Dr. Wangcun Jia and his students for providing the in-vivo window chamber model.

Dr. Bahman Anvari for his guidance, patience, and generosity, which has made this dissertation possible.

The text of this dissertation, in part or in full, is a reprint of the material as it appears in the April 2019 issue of IEEE Transactions on Biomedical Engineering. The co-author Bahman Anvari listed in that publication directed and supervised the research which forms the basis for this dissertation.

ABSTRACT OF THE DISSERTATION

Red-Cell-Derived Contrast Delivery Vehicles for Biomedical Imaging

by

Jack Tang
Doctor of Philosophy, Graduate Program in Bioengineering
University of California, Riverside, December 2019
Dr. Bahman Anvari, Chairperson

Red blood cells (RBCs) have potential as drug carriers for the extended delivery of diagnostic and therapeutic cargos due to the presence of immunomodulatory proteins on their membrane surface. RBC carriers can be used to deliver a variety of diagnostic and/or therapeutic payloads, including small molecule drugs, macromolecular therapeutics, and contrast agents. We encapsulate the FDA-approved NIR-fluorescent dye, indocyanine green (ICG), within the membranes of RBC ghosts and evaluate the potential of such a construct for biomedical fluorescence imaging. These ICG-loaded, RBC-derived constructs are hereon referred to as NIR erythrocyte-mimicking transducers (NETs).

First, we characterize the material properties of micron-sized (μNETs) and nano-sized NETs (nNETs), which have respective relevance in vascular imaging, and cancer imaging. We demonstrate that their absorption and fluorescence characteristics can be optimized for specific imaging system specifications by adjusting the concentation of ICG used to fabricate them. We maximized the fluorescence signal of μNETs and nNETs by loading them using a hypotonic solution containing 20 μM ICG. Our data also provide some insight regarding the localization of ICG to the phospholipid membrane of NETs. We then

demonstrate the fluorescence stability of NETs at specific temperatures that mimic storage (4°C) and usage conditions (37°C).

We further investigate the effect of frozen storage (-20°C) on extruded nano-sized NETs. We observed that size, zeta potential, absorption, and fluorescence properties of extruded nNETs did not change upon thawing after eight weeks of frozen storage. We then tested their uptake in SKOV3 cancer cells, and their biodistribution in Swiss Webster mice and found similar performance between frozen and non-frozen nNETs.

Lastly, we determine that NETs display phosphatidylserine (PS), a known marker of senescence, on their membrane surface. Presence of surface-exposed PS can potentially reduce the circulation time of NETs. We then introduce a new method to potentially increase the circulation half-life of NETs in vivo. We demonstrate partial confinement of PS to the inner leaflet of NETs by enriching their membranes with cholesterol. We demonstrate reduced uptake of cholesterol-enriched NETs by macrophages, which can potentially translate to extended circulation time. We then demonstrate that cholesterol enrichment can prolong the circulation half-life of micron-sized NETs, and discuss the implications of cholesterol-enrichment on nano-sized NETs.

Table of Contents

List of Figures

List of Tables

Chapter 1: Material Properties of NIR Erythrocyte-Mimicking Transducers (NETs)

1.1 Introduction

Exogenous fluorescent materials, which are activated by near-infrared (NIR) excitation (≈700-1450 nm), provides a capability for high-resolution biomedical imaging at the cellular and molecular levels.[1-2]. Such materials can further enhance the imaging contrast as a result of reduced autofluorescence by endogenous molecules over this spectral band.[1] Furthermore, due to the reduced light absorption and scattering by biological constituents, increased depth of optical imaging, on the order of centimeters, can be obtained using NIR wavelengths.[1, 3]

One NIR contrast agent of immense interest is indocyanine green (ICG). It remains as the only FDA-approved NIR fluorophore for specific indications including assessment of cardiac output, hepatic function, and retinal angiography.[4-11] ICG has also been investigated in fluorescence-guided surgery, sentinel lymph node biopsy, and as an agent for photothermal, and photodynamic therapies.[12-26] It is considered one of the least toxic agents administered in humans, having been used in thousands of patients with rare occurrence of side effects (<0.15%).[1, 27]

Despite its established clinical utility, a disadvantage of ICG is its short circulation half-life in circulation (≈2-4 minutes).[28-29] Upon intravenous injection, ICG non-specifically binds to serum proteins, such as albumin, and is uptaken by hepatocytes.[30-32] One strategy for extending the circulation half-life of ICG is to encapsulate it into protective nano-constructs. Various materials have been used to encapsulate ICG, including polymers,

plant-virus capsids, and liposomes.[33-39] Most recently, we have encapsulated ICG into constructs derived from hemoglobin-depleted red blood cells (RBCs), also known as erythrocyte ghosts (EGs).[40-43] We refer to these particles as NIR erythrocyte-mimicking transducers (NETs) since they can convert NIR light into heat, fluorescence, or induce production of cytotoxic agents such as free radicals and singlet oxygen. The utility of erythrocyte-derived particles doped with ICG for imaging and/or phototherapeutic applications has been investigated.[42-47] Erythrocytes-based delivery systems containing other payloads have also been recently reported.[48-50]

There are several advantages to encapsulating ICG within erythrocyte membranes. As constructs that can be fabricated using autologous blood or compatible blood types, NETs may prove to be non-toxic materials for biomedical imaging and therapeutic applications. Furthermore, native RBCs have circulation times on the order of ≈90-120 days, attributed to the presence of specific "self-marker" membrane proteins such as CD47, that allow them to evade cells of the immune system.[51] We have previously demonstrated that CD47 can remain on the surface of NETs, which may provide a mechanism for extended circulation of NETs.[42]

A useful feature of NETs is that their diameter can be tuned to various sizes ranging from nanometer to micrometer scale, and that their ICG content can be adjusted during the fabrication process. Nanometer-sized NETs (nNETs) have relevance to cancer optical theranostics, due to the enhanced permeability and retention (EPR) effect.[52-53] Micrometer-sized NETs (μNETs) can potentially be used for imaging and treatment of vascular diseases, such as port wine stain.

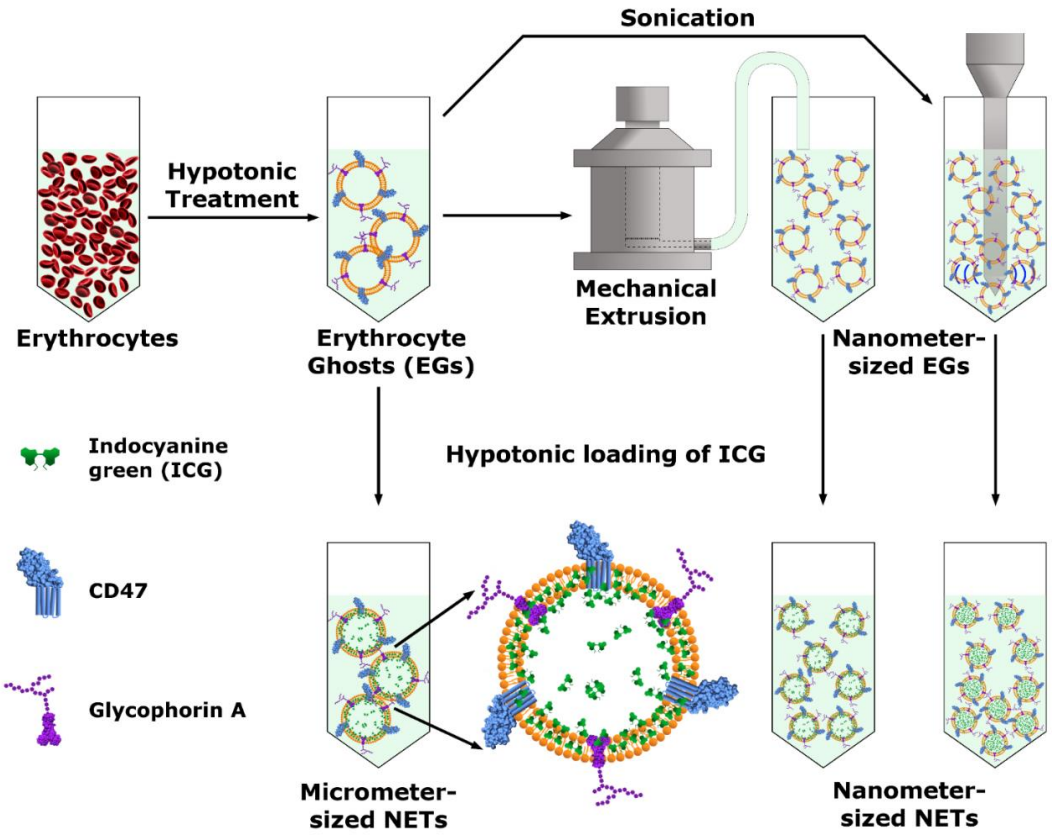

Figure 1. Schematic of the processes to fabricate micrometer- and nanometer-sized NETs (μNETs and nNETs, respectively). After the formation of micrometer-sized erythrocyte ghosts (μEGs), these particles can be loaded with ICG to form μNETs. μEGs are mechanically extruded, or sonicated to reduce their size to the nanometer scale before loading with ICG to yield nNETs.

In this study, we fabricated μNETs, and nNETs formed by two methods based on mechanical extrusion, and sonication (**Figure 1**). Our objective was to investigate the effects of changing the ICG concentration utilized during the fabrication process on the resulting material properties, including zeta potential, ICG loading efficiency, and optical absorption and fluorescence characteristics of both μNETs and nNETs. The fluorescence characteristics are particularly important for clinical translation of NETs for biomedical fluorescence imaging, and provide the basis for selecting an optimized concentration of ICG that can produce μNETs and nNETs with maximal fluorescence emission.

1.2 Results and Discussion

1.2.1 Hydrodynamic diameter and zeta potential (ζ) of NETs.

Based on the dynamic light scattering (DLS) method, the mean intensity-weighted average (z-average) diameter of μNETs ranged between ≈1.9-2.1 μm, depending on the ICG concentration used in the loading buffer (**Figure 2a**). When μNETs were fabricated using ICG loading concentrations in the range of 5-100 μM, the resulting diameters were significantly larger ($p < 0.01$) than that of micrometer-sized erythrocyte ghosts (μEGs). However, the size of μNETs approached a maximum diameter of ≈2.1 μm when using ICG loading concentrations ≥ 20 μM.

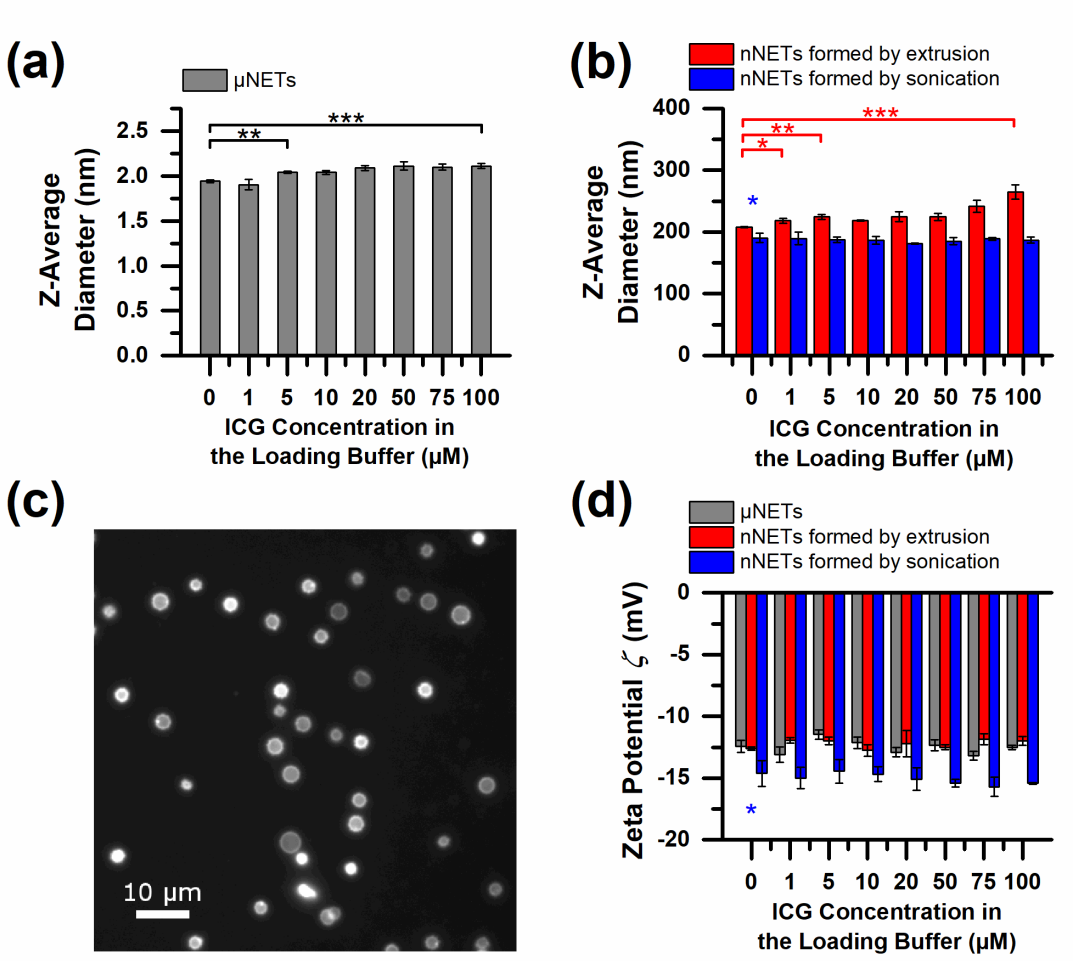

Figure 2. Size and zeta potential of NETs. Z-average diameters were estimated by dynamic light scattering (DLS) for: (a) μEGs and μNETs, and (b) nEGs and nNETs. (c) Fluorescence image of μNETs (100X magnification) formed using 20 μM ICG in the loading buffer. (d) Zeta potential (ζ) of EGs and NETs in 1X (≈300 mOsm) phosphate-buffered saline (PBS). Single, double, and triple asterisks indicate statistically significant differences with $p < 0.05$, 0.01, and 0.001 respectively. In panel (d), the single asterisk indicates statistically significant differences between the ζ values of nEGs formed by sonication, compared to the ζ values of the other two types of NETs.

nNETs formed by extrusion also had significantly larger diameters compared to nEGs, as shown in **Figure 2b**. Depending on the ICG concentration in the loading buffer, z-average diameters of nNETs formed by extrusion ranged between ≈203-255 nm. We have previously published SEM [42] and TEM[43] images of extruded nNETs. In these papers, we demonstrated that electron microscopy and DLS-based measurements of nNETs diameters are in agreement. Estimates of μNETs diameter based on fluorescence microscopy (**Figure 2c**) are also in agreement with DLS-based estimates in **Figure 2a**. We attribute the increase in diameter of μNETs and nNETs formed by extrusion with increased ICG loading concentration to the incorporation of ICG molecules into the phospholipid membrane of NETs. Such localization of the dye may increase the overall diameter of the constructs. Indeed, fluorescence microscopy of μNETs revealed partial localization of ICG to the membrane periphery (**Figure 2c**).

The z-average diameters of nNETs formed by sonication are smaller than the diameter of nNETs formed by extrusion. This is because nEGs formed by the sonication procedure were significantly smaller ($p < 0.05$) than nEGs formed by the extrusion procedure (**Figure 2b**). The mean diameters of nNETs formed by sonication ranged between ≈181-190 nm, and unlike μNETs and nNETs formed by extrusion, did not show a statistically significant dependence on ICG loading concentration. This result suggests that ICG may be primarily localized in the interior of nNETs formed by sonication rather than being embedded within the phospholipid membrane. We attribute this to the disruption and weakening of the membrane and cytoskeleton of EGs during sonication, which may be the physical basis for localization of ICG to the interior cavity.

The ζ values for μNETs and nNETs formed by extrusion were indistinguishable from the ζ of untreated bovine RBCs, which was measured to be -12.78 ± 0.84 mV in 1X PBS (≈300 mOsm) (**Figure 2d**). These results suggest that glycophorin A, and sialic acid, the primary negative charge-bearing components of the RBC membrane, still remain on the RBC membrane after hypotonic treatment or mechanical extrusion.[54]

Preservation of the normal ζ of RBCs can be a contributing factor in increasing the circulation time of NETs. Gbadamosi et al. found a linear relationship between the ζ of methoxyl poly(ethylene glycol)-coated polystyrene microspheres and their uptake by mouse macrophages.[55] Extrapolation of their data shows that ζ of approximately -15 mV would result in minimal uptake by phagocytes. This value is remarkably close to the ζ value of mouse and human RBCs.[56-57] Therefore, NETs and other particle systems with similar ζ, may be minimally uptaken by macrophages as compared to neutral or highly charged particles.[58-59]

All formulations of nNETs formed by sonication had ζ values that were significantly lower ($p < 0.05$) than that of bovine RBCs, μNETs, and nNETs fabricated by extrusion. This may be due to degradation of sialic acid residues or membrane surface proteins during sonication. For the three types of NETs, there were no statistically significant changes in ζ values in response to changes in the ICG concentration within the loading buffer (**Figure 2d**). This result suggests that the sulfonate groups of ICG, which are responsible for the negative net charge of ICG, were completely encapsulated (either localized within the interior cavity or embedded within the membrane), and not exposed to the external environment of the erythrocyte-derived constructs.[60]

Using DLS, Kuo et al. demonstrated that suspensions of nEGs formed by sonication did not aggregate despite freeze-thaw cycling up to five cycles.[61] This was in contrast to liposomal formulations that aggregated after the first freeze-thaw cycle.[61] Our own studies demonstrated that the diameter and ζ of nNETs formed by extrusion did not change even after eight weeks of storage at -20 °C.[62] Therefore, cryopreservation may be a feasible solution for the long-term storage of nNETs, which we will explore in Chapter 2.

1.2.2 Absorption characteristics of NETs

The absorption spectra of μNETs, nNETs formed by extrusion, and nNETs formed by sonication revealed strong NIR absorbance peaks that were centered between 801-805 nm, 797-802 nm, and 799-802 nm, respectively (**Figure 3**). These spectral peaks are attributed to the monomer form of ICG, as indicated in previous studies, and were red-shifted ~20 nm when compared to the absorption peak of free ICG (780 nm).[41-43] This shift is consistent with the behavior of ICG in other micellar systems, and can be attributed to intercalation of ICG into the lipid bilayer of NETs and binding to the phospholipids and membrane proteins therein, leading to changes in the conformation of ICG and its electronic states.[43, 60, 63]

The absorption shoulder in the spectral range of 720-760 nm corresponds to the H-like aggregate form of ICG.[41, 64] This sandwich-like, π-π stacking of individual ICG molecules results in interaction of the individual transition dipole moments that raises the excited-state energy to produce a blue-shifted absorption peak.[37, 64-65] In water, even relatively low concentrations of ICG (> 10 μM) will form H-like aggregates.[64, 66]

As the ICG concentration in the loading buffer increased, there was a corresponding non-linear increase in ICG absorption in the range of 600-900 nm for the three types of NETs. For example, for μNETs (**Figure 3a**), doubling the concentration of ICG in the loading buffer, from 50-100 μM, resulted in an increase in peak NIR absorbance of only 9.4%. For nNETs formed by extrusion (**Figure 3b**), the peak NIR absorbance only increased 27.8% in response to the same increase of 50-100 μM ICG in the loading buffer. For nNETs formed by sonication, this same increase in ICG loading buffer did not change the absorption spectrum (**Figure 3c**). This result suggests that there is a limit to the amount of ICG that can be loaded into NETs. Nevertheless, the nNETs formed by sonication had the highest absorption in the range of 600-900 nm, suggestive of higher loading efficiency of ICG into these nNETs. We present quantitative data regarding ICG loading efficiency in the following section.

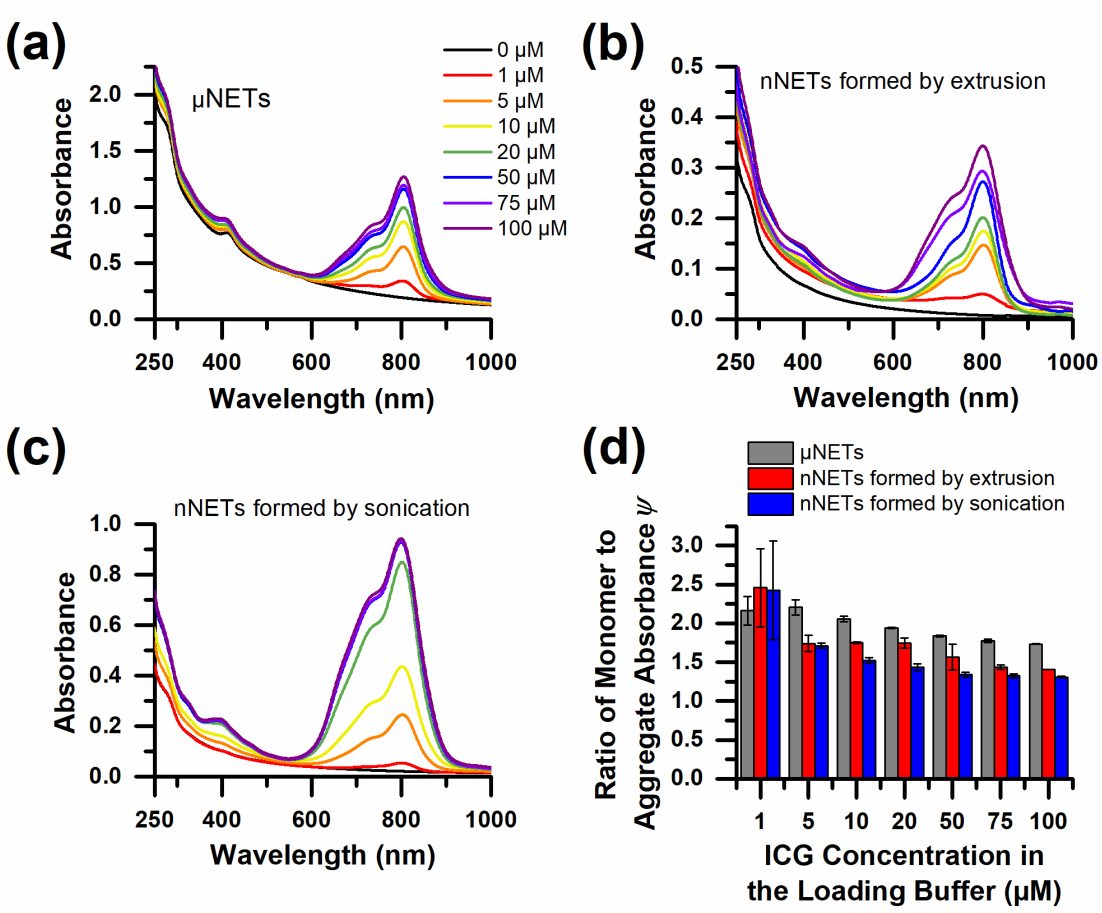

Figure 3. Optical absorption characteristics of NETs. UV-Vis-NIR absorption spectra of: (a) μEGs and μNETs, (b) nEGs and nNETs formed by extrusion, and (c) nEGs and nNETs formed by sonication. In panel (d), we present the ratio of the monomer to H-like aggregate absorbance values of ICG (ψ) [see Equation (1)] for NETs formed using various concentrations of ICG in the loading buffer. The displayed legend (0-100 μM) corresponds to the ICG concentration in the loading buffer to fabricate the three types of NETs and is shared among panels (a), (b), and (c). Each displayed absorption spectrum in panels (a), (b), and (c) is an average of triplicate samples. Error bars in panel (d) are the SDs associated with the triplicate samples of each formulation.

Optical attenuation over the spectral band of 250-500 nm is in part due to scattering by the erythrocyte-derived particles, and absorption by proteins at 280 nm. The presence of ICG also makes small contributions to absorbance values at 280 nm, and 400 nm (data not shown). Despite having nearly the same amount of phospholipid membrane material as μNETs, nNETs formed by sonication showed less attenuation in the 250-500 nm band,

owing to their smaller diameter (**Figure 3c**). In a previous study, we showed that the reduced scattering coefficient of nNETs was less than half (≈45%) of that of μNETs, which is consistent with the lower attenuation in the 250-500 nm spectral band for nNETs formed by sonication.[41] nNETs formed by extrusion had even lower attenuation in this spectral band, due to loss of EG material during the extrusion process, resulting in fewer relative number of light-scattering particles. The lower amount of EG materials in the extruded type is also a contributing factor for their relatively low NIR absorbance and low ICG loading efficiency (**Figure 3b**).

The parameter ψ provides a quantitative measure of the amount of ICG in its monomeric form relative to its H-like aggregate form within the NETs, as described by Equation (1). Values of ψ decreased as the concentration of ICG in the loading buffer increased, indicating progressively higher fractions of the H-like aggregate forms of ICG were present in NETs (**Figure 3d**). The increase in H-like aggregate fractions within NETs is likely due to their presence in the ICG loading buffer prior to being loaded into NETs. At ICG loading concentrations of ≥ 5 μM, values of ψ were highest for μNETs. Thus, the relative fractions of the monomeric form of ICG in μNETs was higher those in nNETs formed by either sonication or extrusion. This behavior influences the fluorescence properties of NETs, as shown later in the text.

1.2.3 ICG loading efficiency of NETs and equivalent free-ICG concentrations

We estimated the loading efficiencies of ICG into NETs (ε) using Equation (2). For all three types of NETs, there was a monotonic decrease in ε as the ICG concentration in the loading buffer was increased beyond 1 μM (**Figure 4a**). The average value of ε for μNETs,

and nNETs formed by extrusion or sonication methods were 87%, 94%, and 98% respectively when using 1 μM ICG concentration in the loading buffer (**Figure 4a**) The low values of ε associated with use of higher concentrations of ICG can be attributed to the fixed amount of EG material available to accept ICG. At high loading concentrations of ICG, the fixed amount of EG material can only uptake a limited amount of ICG, leaving a large fraction of non-encapsulated ICG in the loading buffer.

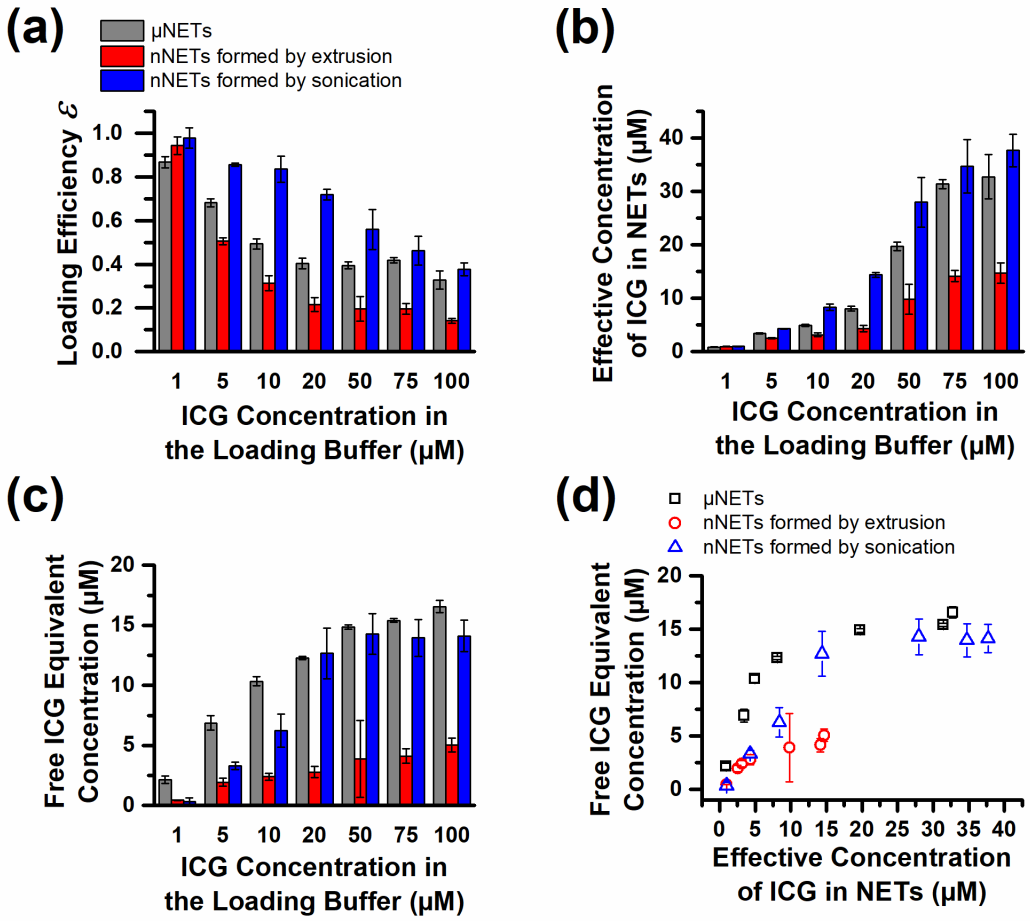

Figure 4. ICG-loading characteristics of NETs. (a) ICG loading efficiency (ε) into NETs [see Equation (2)]. (b) Effective concentration of ICG within NETs. (c) Free ICG equivalent concentration of NETs as functions of ICG concentration of the loading buffer were determined by quantifying the amount of ICG in the supernatant. (d) The free ICG equivalent concentration corresponding to various effective concentrations of ICG within NETs. Error bars in each panel indicate the SDs associated with triplicate samples.

Notably, nNETs formed by sonication had significantly higher ε values ($p < 0.05$) for all ICG loading concentrations when compared to ε for μNETs, and nNETs formed by extrusion (except nNETs formed by extrusion using 1 μM ICG loading concentration). This is likely the result of the aforementioned sonication-induced disruption of the cytoskeletal network and membrane of EGs, which may allow ICG to be more readily loaded. The ε values for nNETs formed by extrusion were significantly lower ($p < 0.05$) than those of other types of NETs, which may be attributed to the lower amount of EG material that remained after the extrusion process.

Multiplying ε by the concentration of ICG in the loading buffer yields the effective concentration of ICG within the population of NETs (**Figure 4b**). Thus, the effective concentration of ICG within NETs is an estimate of the concentration of ICG that would be dispersed in solution if NETs were disintegrated to release their ICG content. The effective concentration of ICG within NETs increased almost sigmoidally toward a maximum limit.

The maximum free ICG equivalent concentrations corresponding to μNETs, and nNETs formed by sonication or extrusion at various ICG loading concentrations were 16.6 ± 0.5, 14.1 ± 1.3, and 5.0 ± 0.6 μM, respectively (**Figure 4c**). Much like the effective concentration of ICG within NETs, the asymptotic trend in free ICG equivalent concentration also indicated a maximum upper limit to the NIR absorbance of NETs.

Values of the free ICG equivalent concentration of NETs, as a function of the effective concentration ICG within NETs are presented in **Figure 4d**. These particular results provide a convenient method to quantitatively determine how the effective ICG

concentration within NETs compares with various concentrations of free ICG dissolved in water. As the loaded concentration of ICG continued to increase beyond 10 μM for nNETs fabricated by extrusion, and 15 μM for μNETs and nNETs formed by sonication, there were nearly no further changes in the free ICG equivalent concentrations. This results suggests that at higher ICG loading concentrations, the additional ICG loaded into NETs was likely in the H-like aggregate form and is consistent with the trend of lower ψ values when increasing the ICG loading concentration (**Figure 3d**).

1.2.4 Fluorescence characteristics of NETs

Normalized excitation emission (ExEm) maps of NETs were calculated using Equation (3) based on absorption and fluorescence spectral data, and are presented as **Figure 5**. We attribute the emission "hot spots" in the range of ≈770-830 nm to the monomeric forms of ICG within NETs. The most intense monomeric emissions were observed from μNETs and nNETs formed by sonication using 5 μM ICG loading concentration when photo-excited at 778 nm and 780 nm, respectively (**Figure 5a, c**). Interestingly, 5 μM corresponded to the ICG concentration at which the maximum value of ψ for μNETs was determined (**Figure 3d**). nNETs formed by extrusion had the highest normalized fluorescence emission intensity value (F) associated with monomeric ICG when they were fabricated using 20 μM of ICG in the loading buffer and photo-excited at 780 nm (**Figure 5b**).

A general trend associated with all three types of NETs is that increasing the concentration of ICG in the loading buffer beyond their respective values associated with maximum monomeric emission as indicated above, produced a second emission hot spot associated with the H-like aggregate emission. Peak values of F associated with H-like

aggregate emissions were produced using respective ICG loading concentrations of 75, 75, and 100 µM for µNETs, and nNETs formed by extrusion or sonication. The corresponding photo-excitation wavelengths for these formulations were 678, 678, and 676 nm, respectively.

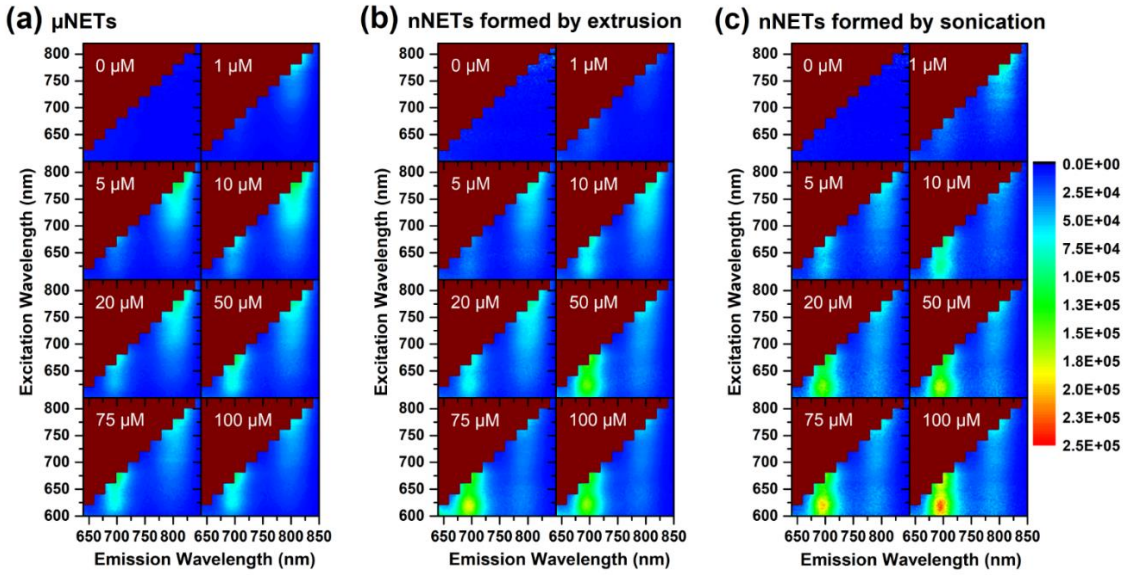

Figure 5. Normalized excitation-emission (ExEm) maps for: (a) µNETs, (b) nNETs formed by extrusion, and (c) nNETs formed by sonication. NETs were fabricated using ICG concentrations in the range of 0-100 µM. Each displayed ExEm map is an average of three ExEm maps generated using triplicate samples. The scale bar on the right corresponds to the values of F, [see Equation (3)].

Using Equation (4), we determined the formulations of NETs that generated maximum fluorescence emission for the detection bands used in the FLARE™ intraoperative imaging system.[17] To do this, we defined parameter γ as the integrated normalized emission collected over the excitation and emission wavelengths used by the system. The two excitation bands were 656-678 nm and 745-779 nm, whereas the two emission collection bands were 689-725 nm and 800-848 nm.

µNETs with the highest average γ were fabricated using 10 µM ICG in the loading buffer (**Figure 6a**). This formulation had a γ value that was statistically different from those

associated with the 1 and 100 μM ICG loading concentrations. nNETs formed by either extrusion or sonication had a maximum average γ when fabricated using 20 μM ICG. We also determined that the maximal values of γ for the three types of NETs fabricated using 20 μM ICG were not statistically different from each other. Therefore, the γ of μNETs and nNETs is maximized when fabricating them using 20 μM ICG in the loading buffer. The corresponding free ICG equivalent concentrations for these formulations were 12.3 ± 0.1, 2.8 ± 0.5, and 13 ± 2 μM for μNETs, nNETs formed by extrusion, and nNETs formed by sonication (**Figure 4c**).

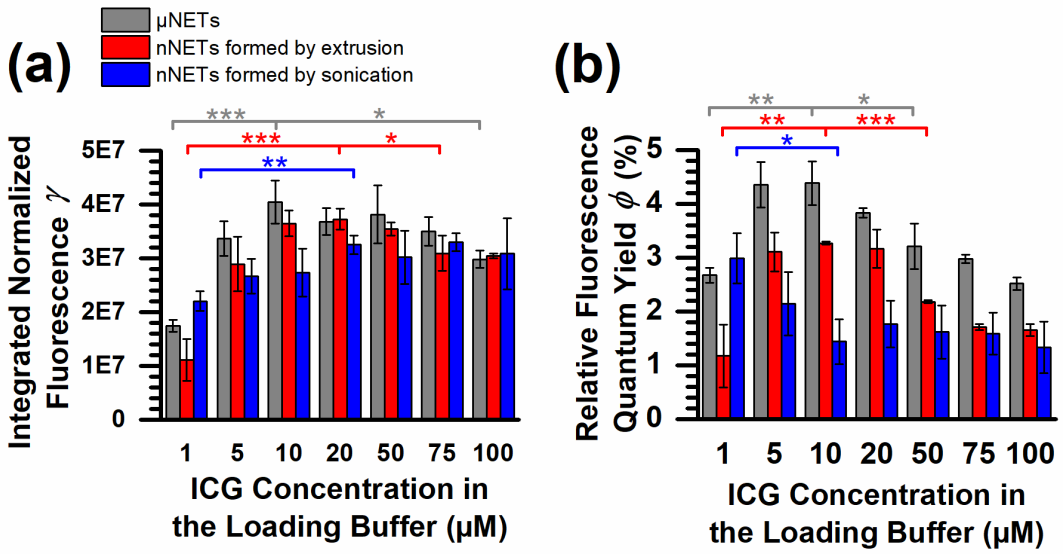

Figure 6. Integrated normalized fluorescence emission [see Equation (4)], and relative fluorescence quantum yield [see Equation (5)] of NETs. (a) Values of the integrated normalized fluorescence emission, γ, and (b) relative fluorescence quantum yield, ϕ, as a function of ICG concentration in the loading buffer for the three types of NETs. Values of ϕ are calculated relative to the ϕ of 6.45 μM free ICG in water, in response to excitation at 780 nm. Single, double, and triple asterisks indicate differences of $p < 0.05$, 0.01, and 0.001, respectively. Error bars indicate the SDs associated with triplicate samples.

Using Equation (5), we determined the relative fluorescence quantum yield, ϕ, of NETs in response to excitation at 780 nm, using 6.45 μM ICG dissolved in water as the reference sample for quantum yield calculations.[63] The maximum values of ϕ obtained for μNETs,

nNETs formed by extrusion, and nNETs formed by sonication were 4.38%, 3.27%, and 2.98%, respectively (**Figure 6b)**. The ICG concentrations used to fabricate NETs with maximum ϕ were 10, 10, and 1 μM for μNETs, nNETs formed by extrusion, and nNETs formed by sonication, respectively. Encapsulation of ICG into NETs resulted in ϕ values that were up to ≈70, 27, and 16% higher than those for free ICG for μNETs, and nNETs formed by extrusion or sonication, respectively.

The increase in ϕ upon encapsulation of ICG into NETs can be attributed to the change in the local environment of ICG. Free ICG has a low ϕ, partly due to its flexible polyene bridge that can rotate and fold in many directions, which can disspitate the excited state energy as heat, instead of fluorescence.[67-68] ICG, among other cyanine dyes, is also prone to aggregation and self-quenching, which can also reduce ϕ.[60, 69-70] Physical association of ICG molecules with NETs constituents (e.g., phospholipids and membrane proteins) derived from erythrocytes can stabilize the polyene bridges and reduce the rate of vibrational relaxation from the excited state, which can lead to increased ϕ. We summarize key optical and material properties of the three types of fluorescence-optimized NETs in Table 1.

1.3 Conclusion

We have fabricated micrometer-sized NETs (μNETs), and nanometer-sized NETs (nNETs) formed by either mechanical extrusion or sonication of erythrocyte ghosts, and characterized several of their key material properties as a function of ICG loading concentration.

Table 1. Material properties of NETs fabricated using 20 μM ICG

Type of NETs	Z-average diameter (nm)	ζ (mV)	ε (%)	ϕ (%)
μNETs	2090 ± 30	-12.9 ± 0.4	40 ± 2	3.83 ± 0.09
nNETs formed by extrusion	225 ± 8	-12 ± 1	22 ± 3	3.2 ± 0.4
nNETs formed by sonication	181.1 ± 0.5	-15.1 ± 0.9	72 ± 2	1.76 ± 0.4

For the Z-average diameter and ζ, the uncertainty values indicate the SD of triplicate samples, where each sample was measured eight times and averaged to obtain a single value. The uncertainty of the estimated ε and ϕ values indicate the SD associated with single measurements of triplicate samples.

μNETs and nNETs formed by extrusion retained the zeta potential (ζ) of native erythrocytes (≈-12 mV in 1X PBS), whereas nNETs formed by sonication had a statistically significant decrease in ζ (≈-15 mV in 1X PBS). This decrease in ζ suggests degradation of erythrocytes membrane materials (e.g., sialic acid or membrane proteins) due to the sonication process. Nevertheless, ζ did not significantly vary with ICG concentration, suggesting that the negatively-charged ICG molecules were fully encapsulated within the three types of NETs. We determined that 20 μM ICG utilized in fabricating NETs presents an optimum concentration that maximizes the integrated fluorescence emission for μNETs and nNETs despite statistically significant differences in their ICG loading efficiency when applied at this concentration. NETs fabricated using 20 μM ICG had fluorescence quantum yields that were 70, 27, and 16% greater than that of free-ICG when encapsulated into in μNETs and nNETs formed by extrusion or sonication, respectively. Our results guide the engineering of NETs with maximal NIR fluorescence emission for specific biomedical imaging applications such as fluorescence-guided tumor resection, and real-time angiography.

1.4 Experimental

1.4.1 Formation of micrometer-sized erythrocyte ghosts (μEGs)

Intact RBCs were isolated from whole bovine blood (1 ml) (Rockland Immunochemicals, Inc., Limerick, PA, USA) in citrate by centrifugation (1000 × g, 5 minutes, 4 °C) (Eppendorf 5424 Microcentrifuge, Hamburg, Germany). The supernatant containing the plasma and buffy coat was discarded, and the erythrocytes were re-suspended in 1 ml of ≈300 mOsm phosphate-buffered saline (1X PBS) (Fisher Bioreagents, Fair Lawn, New Jersey, USA). Erythrocytes were isolated by centrifugally washing them three times in 1X PBS (1000 × g, 5 minutes, 4 °C).

To remove intracellular hemoglobin, the isolated RBCs were incubated in increasingly hypotonic conditions. Specifically, we incubated the RBCs for 20 minutes in 0.5X PBS (1 ml, 4 °C). These RBCs were then collected by centrifugation (20,000 × g, 15 minutes, 4 °C), and the red supernatant (containing hemoglobin and other intracellular contents) was discarded. The pellet of these erythrocytes with partial hemoglobin depletion was then re-suspended in 1 ml of 0.5X PBS. This hypotonic treatment in 0.5X PBS was repeated a total of three times. Then, we decreased the tonicity of the buffer, and re-suspended the erythrocytes in 0.25X PBS and incubated them for 20 minutes at 4 °C. Then, the particles were centrifugally washed (20,000 × g, 15 minutes, 4 °C). Hypotonic treatment and wash in 0.25X PBS was repeated a total of three times.

Hemoglobin-depleted EGs were then resealed by centrifugally washing the pellet in 1X PBS (20,000 × g, 15 minutes, 4 °C), and re-suspending the pellet in 1X PBS. The resulting

micrometer-sized EGs (μEGs) were diluted to have an absorbance value of two at 280 nm, corresponding to ≈0.04 ml of μEGs used for each 1 ml of NETs. The 280 nm wavelength corresponds to the absorption peak of the aromatic rings found in proteins, which enabled us to control the amount of EG material in each sample.

1.4.2 Sonication and mechanical extrusion of μEGs to form nEGs

We reduced the size of μEGs to the nanometer-scale using two methods: sonication and mechanical extrusion (**Figure 1.1**). Under the sonication method, μEGs were subject to ultrasonic pulses in a borosilicate glass vial for eight minutes (30 W, 20 kHz) using a Misonix S-400 probe sonicator (Farmingdale, NY, USA). Each pulse lasted 5 seconds, and pulses were delivered 20 seconds apart. To avoid heating of the EGs, the vial containing the solution was placed in a beaker of ice water during sonication. We replaced the ice after each minute of sonication. After every two minutes of sonication, the EGs were given five minutes to rest in fresh ice water. After sonication was completed, the nanometer-sized EGs (nEGs) were centrifugally washed (100,000 × g, one hour, 4 °C) in a Type 90ti rotor (Beckman Coulter, Inc., Palo Alto, CA, USA) and re-suspended in 1X PBS.

Under the extrusion method, μEGs were sequentially extruded at least five times through track-etched polyester membranes (Sterlitech Corp., Kent, WA, USA) with defined pore diameters (800, 400, and 200 nm) to form nanometer-sized EGs (nEGs). To prevent excessive clogging of the pores, μEGs were diluted prior to extrusion and re-concentrated afterwards. Extrusion was performed using a 10 ml LIPEX® extruder (TRANSFERRA Nanosciences Inc., Burnaby, B.C., Canada). Extruded nEGs were then centrifugally

washed (100,000 × g, one hour, 4 °C), and re-suspended in their original volume of 1X PBS.

1.4.3 Loading μEGs and nEGs with ICG to form NETs

Each type of EG (micrometer-, and nanometer-sized formed by sonication or extrusion) was loaded with ICG by incubating the EGs in a hypotonic solution containing ICG. The ICG loading buffer contained a 1:1:1 volume ratio of EGs, Sorenson's phosphate buffer (0.1 M, pH 7.4), and a known concentration of aqueous ICG. We varied the total concentration of the ICG loading buffer (0, 1, 5, 10, 20, 50, 75, and 100 μM) and incubated the EGs with the indicated ICG loading buffers for 30 minutes to form NETs. The total tonicity of the ICG loading buffers were ≈175 mOsm.

Following incubation, excess ICG was removed by centrifugation (20,000 × g, 15 minutes for μNETs; 100,000 × g, one hour for nNETs formed by sonication or extrusion). The supernatant was set aside to quantify the loading efficiency of ICG into NETs (as described below). The resulting NETs were then washed in 3 ml of 1X PBS to reseal the membranes and remove residual ICG. The supernatant from this wash was removed and added to the supernatant for quantification of the ICG loading efficiency of NETs. NETs were then re-suspended in 1 ml of 1X PBS for characterization studies.

1.4.4 DLS measurement of NETs diameters and zeta potential

The hydrodynamic diameters of each NETs formulation was measured by dynamic light scattering (DLS) using a Malvern Zetasizer NanoZS (Malvern, United Kingdom). Samples were suspended in 1 ml 1X PBS within a polystyrene cuvette (1 cm pathlength). Each DLS measurement was collected at 90° scattering angle. We report the size of NETs

using the z-average diameter, which is the intensity-based harmonic mean of the light-scattering particles.[71-72] Eight measurements were taken for each sample, and averaged. The average diameters of three independent samples were then used to calculate the mean z-average diameter and the corresponding standard deviation (SD).

The zeta potential (ζ) of NETs and EGs in 1X PBS were also estimated using the Malvern Zetasizer via the Smoluchowski approximation, which relates the ζ to the observed electrophoretic mobility of the particles.[73-74] Each measurement was done in a folded capillary cell at 10 °C. Similar to the z-average diameter characterizations, the ζ of each formulation of NETs was measured eight times, and averaged. This was done for three independent samples, and used to estimate the mean ζ and the corresponding SD.

1.4.5 Fluorescence microscopy of μNETs

Fluorescence images of μNETs were obtained using a Hamamatsu C9100-13 electron-multiplying charge-coupled detector (Hamamatsu, Japan) with a Nikon Eclipse Ti microscope (Tokyo, Japan) and a Chroma Li-Cor IR800 filter cube (Bellows Falls, Vermont, USA). We used a Nikon objective lens with 100x magnification (Tokyo, Japan). The excitation band was 740 ± 20 nm, and the emission was passed through a filter transmitting wavelengths greater than 780 nm.

1.4.6 UV-vis-NIR absorption spectra of NETs

Steady-state absorption spectra of each formulation of NETs was recorded using a UV-Vis-NIR spectrophotometer (JASCO V-670, Tokyo, Japan) in transmission mode with a quartz absorbance microcuvette (1 cm pathlength). The spectral range for all absorbance

measurements was from 230-1100 nm to ensure that both the UV and NIR absorption, from proteins and ICG respectively, were recorded.

The spectral features of ICG provide insight into the conformational states of ICG present within NETs. ICG can be in either a monomeric form, indicated by an absorption peak at 805 nm, or in an H-like aggregated form, indicated by a secondary absorption peak at 740 nm.[64-65] We define the parameter ψ as the ratio of the monomeric ICG absorbance to that of the H-like aggregate form of ICG. We note that the "absorption" of NETs is effectively a combination of optical scattering and photon absorption. Therefore, the spectra of EGs (formed using 0 μM ICG in the loading buffer) contains both the optical scattering component of the particles, as well as the absorption component of proteins and any residual hemoglobin. To calculate ψ, we first removed the contribution of optical scattering and absorption by other components in NETs by subtracting the baseline absorption spectrum of EGs (constructs without ICG) from each absorption spectrum of NETs. Then, we used this baseline-subtracted absorbance for the calculation of ψ, as:

$$\psi = \frac{A^*(\lambda = 805 \text{ nm})}{A^*(\lambda = 740 \text{ nm})} \qquad (1)$$

where A*(λ = 805 nm) is the absorbance value of NETs at 805 nm minus the absorbance value of EGs at 805 nm. Similarly, $A^*(\lambda = 740 \text{ nm})$ is the absorbance value of NETs at 740 nm minus the absorbance value of EGs at 740 nm. Wavelength is denoted as λ.

1.4.7 Quantification of ICG loading efficiency of NETs

We define the ICG loading efficiency (ε) of NETs as:

$$\varepsilon = 1 - \frac{m_{\text{super}}}{m_{\text{initial}}} \qquad (2)$$

where m_{initial} is the amount of ICG introduced into the loading buffer, and m_{super} is the amount of ICG present in the supernatant upon completing the fabrication of NETs. The supernatant was collected immediately after centrifugation and stored in a dark refrigerator at 4°C to prevent ICG photobleaching. Supernatant solutions were contained in disposable polystyrene cuvettes (1 cm pathlength), and their absorption spectra (400-1100 nm) were obtained using the UV-vis-NIR spectrophotometer. To determine m_{super}, we compared the absorbance value of the supernatant at its spectral peak (780 nm) to a calibration curve (data not shown) that related peak absorbance values of supernatant ICG to known concentrations of ICG in the same supernatant buffer.

Currently, the clinical formulation of ICG is free ICG dissolved in water. In order to compare the optical absorption of NETs with that of free ICG in water, we determined the equivalent concentration of free ICG that would have the same monomer absorbance value as each of the NETs formulations fabricated using various ICG concentrations in the loading buffer. To do this, we first subtracted the baseline spectrum of EGs (i.e., particles not loaded with ICG) from the absorption spectrum of each formulation of NETs. In this manner, we eliminated the contribution of optical scattering and protein absorption from each spectrum. We then compared the monomeric absorption peaks of baseline-subtracted NETs to a calibration curve of the monomeric absorption peaks of free ICG dissolved in water, in the range of ≈1-26 μM, to determine the equivalent free ICG concentration of NETs.

1.4.8 Excitation-emission mapping of NETs fluorescence

To determine the fluorescence characteristics of each formulation of NETs, we mapped the excitation-emission (ExEm) spectra using a Fluorolog-3 spectrofluorometer (HORIBA, Ltd., Edison, New Jersey, USA). Solution of NETs were contained within a quartz cuvette (1 cm pathlength). The excitation wavelengths ranged between 600-830 nm, and were generated using a 450 W xenon arc lamp. Corresponding to each excitation wavelength, the bathochromic fluorescence light was collected by the detector to ensure the collection of only the fluorescence, but not the scattered light.

Prior to ExEm mapping, a sample of each NETs formulation was diluted to have a NIR peak absorbance of 0.2 or lower. This minimized measurement errors originating from the primary inner-filter effect, which describes the inability of excitation light to propagate through the entire cuvette pathlength in strongly absorbing samples.[75] We also compensated for the inner-filter effect mathematically, by normalizing fluorescence intensity values (*f*) in each ExEm map with respect to the percentage of excitation light absorbed by the sample, as:

$$F(\lambda_{ex}, \lambda_{em}) = \frac{f(\lambda_{ex}, \lambda_{em})}{1 - 10^{-A_{ex}}} \qquad (3)$$

where, $F(\lambda_{ex}, \lambda_{em})$ is the normalized fluorescence emission, λ_{ex} is a given excitation wavelength, λ_{em} is an emission wavelength in response to excitation at λ_{ex}, and A_{ex} is the absorbance of the diluted NETs formulation at λ_{ex}.

To obtain an estimate of total fluorescence emission for a given NETs formulation, we integrated the emission in response to two bands of excitation wavelengths, 656-678 nm and 745-779 nm. We chose these particular bands since they correspond to the excitation

light sources utilized in a clinically relevant NIR intraoperative fluorescence imaging system, the FLuorescence-Assisted Resection and Exploration (FLARE™) system.[17] The system consists of two LED sources for NIR excitation in bands of 656-678 nm and 745-779 nm. Fluorescence emission passed through two NIR filters with respective bandpass wavelengths of 689-725 nm and 800-848 nm. Mathematically, we defined γ, the integrated normalized fluorescence emission, as:

$$\gamma = \sum_{\lambda_{ex}=656\text{ nm}}^{\lambda_{ex}=678\text{ nm}} \left[\int_{\lambda_{em}=689\text{ nm}}^{\lambda_{em}=725\text{ nm}} F(\lambda_{ex}, \lambda_{em})\, d\lambda_{em} + \int_{\lambda_{em}=800\text{ nm}}^{\lambda_{em}=848\text{ nm}} F(\lambda_{ex}, \lambda_{em})\, d\lambda_{em} \right] + \sum_{\lambda_{ex}=745\text{ nm}}^{\lambda_{ex}=779\text{ nm}} \left[\int_{\lambda_{em}=800\text{ nm}}^{\lambda_{em}=848\text{ nm}} F(\lambda_{ex}, \lambda_{em})\, d\lambda_{em} \right] \quad (4)$$

We also determined the relative fluorescence quantum yield (ϕ_{NETs}) for each of the NETs formulations in response to 780 nm excitation wavelength, which corresponds to the absorption peak of free ICG, as:

$$\phi_{NETs}(\lambda_{ex}) = \phi_{ICG}(\lambda_{ex}) \times \left[\frac{\int_{\lambda_{em}=800\text{ nm}}^{\lambda_{em}=850\text{ nm}} f_{NETs}(\lambda_{ex}, \lambda_{em}) d\lambda_{em}}{1 - 10^{-A_{NETs}(\lambda_{ex})}} \right] \times \left[\frac{1 - 10^{-A_{ICG}(\lambda_{ex})}}{\int_{\lambda_{em}=800\text{ nm}}^{\lambda_{em}=850\text{ nm}} f_{ICG}(\lambda_{ex}, \lambda_{em}) d\lambda_{em}} \right] \quad (5)$$

where λ_{ex} = 780 nm, $\phi_{ICG}(\lambda_{ex})$ is the fluorescence quantum yield (≈ 2.58%) of free ICG in water (6.45 μM) at 780 nm excitation wavelength, $f_{NETs}(\lambda_{ex}, \lambda_{em})$ is the fluorescence emission intensity of a given NETs formulation in response to 780 nm excitation, $A_{NETs}(\lambda_{ex})$ is the absorbance value of a given NETs formulation at 780 nm, $A_{ICG}(\lambda_{ex})$ is the absorbance value of free ICG in water (6.45 μM) at 780 nm, and $f_{ICG}(\lambda_{ex}, \lambda_{em})$ is the

fluorescence emission intensity of free ICG in water (6.45 μM) in response to 780 nm excitation wavelength.[63]

1.5 References

1. Frangioni, J. V., In vivo near-infrared fluorescence imaging. *Curr. Opin. Chem. Biol.* **2003,** *7* (5), 626-634.

2. Gibbs, S. L., Near infrared fluorescence for image-guided surgery. *Quant. Imaging Med. Surg.* **2012,** *2* (3), 177-187.

3. Lin, M. Z., Beyond the rainbow: new fluorescent proteins brighten the infrared scene. *Nat. Methods* **2011,** *8* (9), 726-728.

4. Miller, D. E.; Gleason, W. L.; Mcintosh, H. D., Comparison of cardiac output determination by direct Fick method and dye-dilution method using indocyanine green dye and a cuvette densitometer. *J. Lab. Clin. Med.* **1962,** *59* (2), 345-350.

5. Weis, F.; Kilger, E.; Beiras-Fernandez, A.; Hinske, C. L.; Nassau, K.; Adnan, L.; Vicol, C.; Kur, F.; Mohnle, P., Indocyanine green clearance as an outcome prediction tool in cardiac surgery: a prospective study. *J. Crit. Care.* **2014,** *29* (2), 224-229.

6. Jochum, C.; Beste, M.; Penndorf, V.; Farahani, M. S.; Testa, G.; Nadalin, S.; Malago, M.; Broeisch, C. E.; Gerken, G., Quantitative liver function tests in donors and recipients of living donor liver transplantation. *Liver Transplant.* **2006,** *12* (4), 544-549.

7. Afonso, S.; Miranda, I.; Matos, R.; Moreno, R.; Amado, P.; Martins, F. O., The use of indocyanine green in the evaluation of hepatic function before and after hepatic resection surgery. *Intensive Care Med.* **2009,** *35*, 130.

8. Mohnle, P.; Kilger, E.; Adnan, L.; Beiras-Fernandez, A.; Vicol, C.; Weis, F., Indocyanine green clearance after cardiac surgery: the impact of cardiopulmonary bypass. *Perfusion* **2012,** *27* (4), 292-299.

9. Lima, M. D.; Bartsch, D. U.; Freeman, W. R.; Weinreb, R. N., Indocyanine green angiography of optic disc and peripapillary retina in glaucoma. *Invest. Ophth. Vis. Sci.* **1996,** *37* (3), 1007.

10. Hochheimer, B. F., Angiography of retina with indocyanine green. *Arch. Ophthalmol.* **1971,** *86* (5), 564-565.

11. Fineman, M. S.; Maguire, J. I.; Fineman, S. W.; Benson, W. E., Safety of indocyanine green angiography during pregnancy - a survey of the retina, macula, and vitreous societies. *Arch. Ophthalmol.* **2001,** *119* (3), 353-355.

12. Siddighi, S.; Yune, J. J.; Hardesty, J., Indocyanine green for intraoperative localization of ureter. *Am. J. Obstet. Gynecol.* **2014,** *211* (4), 436.e1-436.e2.

13. Boni, L.; David, G.; Mangano, A.; Dionigi, G.; Rausei, S.; Spampatti, S.; Cassinotti, E.; Fingerhut, A., Clinical applications of indocyanine green (ICG) enhanced fluorescence in laparoscopic surgery. *Surg. Endoscopy* **2015,** *29* (7), 2046-2055.

14. Alander, J. T.; Kaartinen, I.; Laakso, A.; Patila, T.; Spillmann, T.; Tuchin, V. V.; Venermo, M.; Valisuo, P., A review of indocyanine green fluorescent imaging in surgery. *Int. J. Biomed. Imaging* **2012,** *2012*, 940585.

15. Chen, S. L.; Iddings, D. M.; Scheri, R. P.; Bilchik, A. J., Lymphatic mapping and sentinel node analysis: current concepts and applications. *CA Cancer J. Clin.* **2006,** *56* (5), 292-309.

16. Isei, T.; Okamoto, H., Fluorescence navigation with indocyanine green for sentinel lymph node biopsy in acral melanoma and genital extramammary Paget's carcinoma. *Ann. Surg. Oncol.* **2008,** *15*, 58-59.

17. Troyan, S. L.; Kianzad, V.; Gibbs-Strauss, S. L.; Gioux, S.; Matsui, A.; Oketokoun, R.; Ngo, L.; Khamene, A.; Azar, F.; Frangioni, J. V., The FLARE intraoperative near-infrared fluorescence imaging system: a first-in-human clinical trial in breast cancer sentinel lymph node mapping. *Ann. Surg. Oncol.* **2009,** *16* (10), 2943-2952.

18. Abe, H.; Mori, T.; Umeda, T.; Tanaka, M.; Kawai, Y.; Shimizu, T.; Cho, H.; Kubota, Y.; Kurumi, Y.; Tani, T., Indocyanine green fluorescence imaging system for sentinel lymph node biopsies in early breast cancer patients. *Surg. Today* **2011,** *41* (2), 197-202.

19. Korn, J. M.; Tellez-Diaz, A.; Bartz-Kurycki, M.; Gastman, B., Indocyanine green SPY elite-assisted sentinel lymph node biopsy in cutaneous melanoma. *Plast. Reconstr. Surg.* **2014,** *133* (4), 914-922.

20. Pitsinis, V.; Provenzano, E.; Kaklamanis, L.; Wishart, G. C.; Benson, J. R., Indocyanine green fluorescence mapping for sentinel lymph node biopsy in early breast cancer. *Surg. Oncol.* **2015,** *24* (4), 375-379.

21. Athiraman, H.; Wolf, R. F.; Bartels, K. E.; Shivakoti, S.; Liu, H.; Chen, W. R., Selective photothermal tissue interaction using 805-nm laser and indocyanine green in tissue welding. *J. X-Ray Sci. Technol.* **2004,** *12* (2), 117-126.

22. Zheng, X. H.; Xing, D.; Zhou, F. F.; Wu, B. Y.; Chen, W. R., Indocyanine green-containing nanostructure as near infrared dual-functional targeting probes for optical imaging and photothermal therapy. *Mol. Pharmaceut.* **2011,** *8* (2), 447-456.

23. Warn, A. A.; Nordquist, R. E.; Chen, W., Photodynamic therapy of subcutaneous and intraocular tumors using indocyanine green. *Invest. Ophth. Vis. Sci.* **1994,** *35* (4), 1924.

24. Urbanska, K.; Romanowska-Dixon, B.; Matuszak, Z.; Oszajca, J.; Nowak-Sliwinska, P.; Stochel, G., Indocyanine green as a prospective sensitizer for photodynamic therapy of melanomas. *Acta Biochim. Pol.* **2002,** *49* (2), 387-391.

25. Sawa, M.; Awazu, K.; Takahashi, T.; Sakaguchi, H.; Horiike, H.; Ohji, M.; Tano, Y., Application of femtosecond ultrashort pulse laser to photodynamic therapy mediated by indocyanine green. *Brit. J. Ophthalmol.* **2004,** *88* (6), 826-831.

26. Seo, H. M.; Min, H. G.; Kim, H. J.; Shin, J. H.; Nam, S. H.; Han, K. S.; Ryu, J. H.; Oh, J. J.; Kim, J. Y.; Lee, K. J.; Lee, S. J.; Kim, H. S.; Kim, J. I.; Song, M. K.; Kim, W. S., Effects of repetitive photodynamic therapy using indocyanine green for acne vulgaris. *Int. J. Dermatol.* **2016,** *55* (10), 1157-1163.

27. Hope-Ross, M.; Yannuzzi, L. A.; Gragoudas, E. S.; Guyer, D. R.; Slakter, J. S.; Sorenson, J. A.; Krupsky, S.; Orlock, D. A.; Puliafito, C. A., Adverse reactions due to indocyanine green. *Ophthalmology* **1994,** *101* (3), 529-533.

28. Desmettre, T.; Devoisselle, J. M.; Mordon, S., Fluorescence properties and metabolic features of indocyanine green (ICG) as related to angiography. *Surv. Ophthalmol.* **2000,** *45* (1), 15-27.

29. Yaseen, M. A.; Yu, J.; Wong, M. S.; Anvari, B., In-vivo fluorescence imaging of mammalian organs using charge-assembled mesocapsule constructs containing indocyanine green. *Opt. Express* **2008,** *16* (25), 20577-20587.

30. Keiding, S.; Ott, P.; Bass, L., Enhancement of unbound clearance of ICG by plasma proteins, demonstrated in human subjects and interpreted without assumption of facilitating structures. *J. Hepatol.* **1993,** *19* (3), 327-344.

31. Ott, P.; Bass, L.; Keiding, S., Hepatic ICG removal in the pig depends on plasma protein and hematocrit: evidence of sinusoidal binding disequilibrium and unstirred water layer effects. *Hepatology* **1997,** *26* (3), 679-690.

32. Yoneya, S.; Saito, T.; Komatsu, Y.; Koyama, I.; Takahashi, K.; Duvoll-Young, J., Binding properties of indocyanine green in human blood. *Invest. Ophth. Vis. Sci.* **1998,** *39* (7), 1286-1290.

33. Fukasawa, T.; Hashimoto, M.; Nagamine, S.; Aoki, H.; Shinto, H.; Ito, S.; Ohshima, M., Fabrication of ICG dye-containing particles by growth of polymer/salt aggregates and measurement of photoacoustic signals. *Chem. Lett.* **2014,** *43* (4), 495-497.

34. Bahmani, B.; Guerrero, Y.; Bacon, D.; Kundra, V.; Vullev, V. I.; Anvari, B., Functionalized polymeric nanoparticles loaded with indocyanine green as theranostic materials for targeted molecular near infrared fluorescence imaging and photothermal destruction of ovarian cancer cells. *Lasers Surg. Med.* **2014,** *46* (7), 582-592.

35. Jung, B. S.; Rao, A. L. N.; Anvari, B., Optical nano-constructs composed of genome-depleted brome mosaic virus doped with a near infrared chromophore for potential biomedical applications. *ACS Nano* **2011,** *5* (2), 1243-1252.

36. Jung, B. S.; Anvari, B., Virus-mimicking optical nanomaterials: near infrared absorption and fluorescence characteristics and physical stability in biological environments. *ACS Appl. Mater. Interfaces* **2013,** *5* (15), 7492-7500.

37. Guerrero, Y.; Singh, S. P.; Mai, T.; Murali, R. K.; Tanikella, L.; Zahedi, A.; Kundra, V.; Anvari, B., Optical characteristics and tumor imaging capabilities of near infrared dyes in free and nano-encapsulated formulations comprised of viral capsids. *ACS Appl. Mater. Interfaces* **2017,** *9* (23), 19601-19611.

38. Jeong, H. S.; Lee, C. M.; Cheong, S. J.; Kim, E. M.; Hwang, H.; Na, K. S.; Lim, S. T.; Sohn, M. H.; Jeong, H. J., The effect of mannosylation of liposome-encapsulated indocyanine green on imaging of sentinel lymph node. *J. Liposome Res.* **2013,** *23* (4), 291-297.

39. Viitala, L.; Pajari, S.; Lajunen, T.; Kontturi, L. S.; Laaksonen, T.; Kuosmanen, P.; Viitala, T.; Urtti, A.; Murtomaki, L., Photothermally triggered lipid bilayer phase transition and drug release from gold nanorod and indocyanine green encapsulated liposomes. *Langmuir* **2016,** *32* (18), 4554-4563.

40. Vankayala, R.; Corber, S. R.; Mac, J. T.; Rao, M. P.; Shafie, M.; Anvari, B., Erythrocyte-derived nanoparticles as a theranostic agent for near-infrared fluorescence imaging and thrombolysis of blood clots. *Macromol. Biosci.* **2018**, 1700379.

41. Burns, J. M.; Saager, R.; Majaron, B.; Jia, W. C.; Anvari, B., Optical properties of biomimetic probes engineered from erythrocytes. *Nanotechnology* **2017,** *28* (3).

42. Mac, J. T.; Nunez, V.; Burns, J. M.; Guerrero, Y. A.; Vullev, V. I.; Anvari, B., Erythrocyte-derived nano-probes functionalized with antibodies for targeted near infrared fluorescence imaging of cancer cells. *Biomed. Opt. Express* **2016,** *7* (4), 1311-1322.

43. Bahmani, B.; Bacon, D.; Anvari, B., Erythrocyte-derived photo-theranostic agents: hybrid nano-vesicles containing indocyanine green for near infrared imaging and therapeutic applications. *Sci. Rep.* **2013,** *3*.

44. Flower, R. W.; Kling, R., Observation and characterization of microvascular vasomotion using erythrocyte mediated ICG angiography (EM-ICG-A). *Microvasc. Res.* **2017,** *113*, 78-87.

45. Agrawal, R.; Balne, P. K.; Tun, S. B. B.; Sia Wey, Y.; Khandelwal, N.; Barathi, V. A., Fluorescent dye labeling of erythrocytes and leukocytes for studying the flow dynamics in mouse retinal circulation. *J. Visualized Exp.* **2017,** (125), e55495.

46. Ren, H.; Liu, J.; Li, Y.; Wang, H.; Ge, S.; Yuan, A.; Hu, Y.; Wu, J., Oxygen self-enriched nanoparticles functionalized with erythrocyte membranes for long circulation and enhanced phototherapy. *Acta Biomater.* **2017,** *59*, 269-282.

47. Wan, G.; Chen, B.; Li, L.; Wang, D.; Shi, S.; Zhang, T.; Wang, Y.; Zhang, L.; Wang, Y., Nanoscaled red blood cells facilitate breast cancer treatment by combining photothermal/photodynamic therapy and chemotherapy. *Biomaterials* **2018,** *155*, 25-40.

48. Piao, J. G.; Wang, L. M.; Gao, F.; You, Y. Z.; Xiong, Y. J.; Yang, L. H., Erythrocyte membrane is an alternative coating to polyethylene glycol for prolonging the circulation lifetime of gold nanocages for photothermal therapy. *ACS Nano* **2014,** *8* (10), 10414-10425.

49. Peng, J. R.; Yang, Q.; Li, W. T.; Tan, L. W.; Xiao, Y.; Chen, L. J.; Hao, Y.; Qian, Z. Y., Erythrocyte-membrane-coated prussian blue/manganese dioxide nanoparticles as H2O2-responsive oxygen generators to enhance cancer chemotherapy/thotothermal therapy. *ACS Appl. Mater. Interfaces* **2017,** *9* (51), 44410-44422.

50. Rao, L.; Meng, Q. F.; Bu, L. L.; Cai, B.; Huang, Q. Q.; Sun, Z. J.; Zhang, W. F.; Li, A.; Guo, S. S.; Liu, W.; Wang, T. H.; Zhao, X. Z., Erythrocyte membrane-coated upconversion nanoparticles with minimal protein adsorption for enhanced tumor imaging. *ACS Appl. Mater. Interfaces* **2017,** *9* (3), 2159-2168.

51. Oldenborg, P. A.; Zheleznyak, A.; Fang, Y. F.; Lagenaur, C. F.; Gresham, H. D.; Lindberg, F. P., Role of CD47 as a marker of self on red blood cells. *Science* **2000,** *288* (5473), 2051-2054.

52. Acharya, S.; Sahoo, S. K., PLGA nanoparticles containing various anticancer agents and tumour delivery by EPR effect. *Adv. Drug Deliv. Rev.* **2011,** *63* (3), 170-183.

53. Li, S. D.; Huang, L., Pharmacokinetics and biodistribution of nanoparticles. *Mol. Pharmaceut.* **2008,** *5* (4), 496-504.

54. Eylar, E. H.; Madoff, M. A.; Oncley, J. L.; Brody, O. V., Contribution of sialic acid to surface charge of the erythrocyte. *J. Biol. Chem.* **1962,** *237* (6), 1992-2000.

55. Gbadamosi, J. K.; Hunter, A. C.; Moghimi, S. M., PEGylation of microspheres generates a heterogeneous population of particles with differential surface characteristics and biological performance. *FEBS Lett.* **2002,** *532* (3), 338-344.

56. Jan, K. M.; Chien, S., Role of surface electric charge in red blood cell interactions. *J. Gen. Physiol.* **1973,** *61* (5), 638-654.

57. Munksgaard, P. S.; Skals, M.; Reinholdt, J.; Poulsen, K.; Jensen, M. R.; Yang, C. X.; Leipziger, J.; Vorup-Jensen, T.; Praetorius, H. A., Sialic acid residues are essential for cell lysis mediated by leukotoxin from aggregatibacter actinomycetemcomitans. *Infect. Immun.* **2014,** *82* (6), 2219-2228.

58. Tan, S. W.; Wu, T. T.; Zhang, D.; Zhang, Z. P., Cell or cell membrane-based drug delivery systems. *Theranostics* **2015,** *5* (8), 863-881.

59. Arvizo, R. R.; Miranda, O. R.; Moyano, D. F.; Walden, C. A.; Giri, K.; Bhattacharya, R.; Robertson, J. D.; Rotello, V. M.; Reid, J. M.; Mukherjee, P., Modulating pharmacokinetics, tumor uptake and biodistribution by engineered nanoparticles. *PLoS One* **2011,** *6* (9), e24374.

60. Kraft, J. C.; Ho, R. J. Y., Interactions of indocyanine green and lipid in enhancing near-infrared fluorescence properties: the basis for near-infrared imaging in vivo. *Biochem.* **2014,** *53* (8), 1275-1283.

61. Kuo, Y. C.; Wu, H. C.; Hoang, D.; Bentley, W. E.; D'Souza, W. D.; Raghavan, S. R., Colloidal properties of nanoerythrosomes derived from bovine red blood cells. *Langmuir* **2016,** *32* (1), 171-179.

62. Tang, J. C.; Mac, J. T.; Vankayala, R.; Partono, A.; Jia, W.; Anvari, B. Effect of freezing on erythrocyte-derived optical nanoprobes. In *Optics in the Life Sciences Congress*, Proceedings of the Optical Society of America, San Diego, CA, Apr 2-5, 2017; 2017; p OmTu2D.4.

63. Kirchherr, A. K.; Briel, A.; Mader, K., Stabilization of indocyanine green by encapsulation within micellar systems. *Mol. Pharmaceut.* **2009,** *6* (2), 480-491.

64. Jung, B. S.; Vullev, V. I.; Anvari, B., Revisiting indocyanine green: effects of serum and physiological temperature on absorption and fluorescence characteristics. *IEEE J. Sel. Top. Quant. Electron.* **2014,** *20* (2), 149-157.

65. Kasha, M., Energy transfer mechanisms and molecular exciton model for molecular aggregates. *Radiat. Res.* **1963,** *20* (1), 55-71.

66. von Berlepsch, H.; Bottcher, C., H-aggregates of an indocyanine Cy5 dye: transition from strong to weak molecular coupling. *J. Phys. Chem. B* **2015,** *119* (35), 11900-11909.

67. Hong, G. S.; Tabakman, S. M.; Welsher, K.; Chen, Z.; Robinson, J. T.; Wang, H. L.; Zhang, B.; Dai, H. J., Near-infrared-fluorescence-enhanced molecular imaging of live cells on gold substrates. *Angew. Chem. Int. Edit.* **2011,** *50* (20), 4644-4648.

68. Benson, R. C.; Kues, H. A., Absorption and fluorescence properties of cyanine dyes. *J. Chem. Eng. Data* **1977,** *22* (4), 379-383.

69. Zhegalova, N. G.; He, S.; Zhou, H. Y.; Kim, D. M.; Berezin, M. Y., Minimization of self-quenching fluorescence on dyes conjugated to biomolecules with multiple labeling sites via asymmetrically charged NIR fluorophores. *Contrast Media Mol. Imaging* **2014,** *9* (5), 355-362.

70. Rosch, U.; Yao, S.; Wortmann, R.; Wurthner, F., Fluorescent H-aggregates of merocyanine dyes. *Angew. Chem. Int. Edit.* **2006,** *45* (42), 7026-7030.

71. Koppel, D. E., Analysis of macromolecular polydispersity in intensity correlation spectroscopy - method of cumulants. *J. Chem. Phys.* **1972,** *57* (11), 4814.

72. Thomas, J. C., The determination of log normal particle size distributions by dynamic light scattering. *J. Colloid Interface. Sci.* **1987,** *117* (1), 187-192.

73. Sze, A.; Erickson, D.; Ren, L. Q.; Li, D. Q., Zeta-potential measurement using the Smoluchowski equation and the slope of the current-time relationship in electroosmotic flow. *J. Colloid Interface Sci.* **2003,** *261* (2), 402-410.

74. Islam, M. A., Einstein-Smoluchowski diffusion equation: a discussion. *Phys. Scripta.* **2004,** *70* (2-3), 120-125.

75. Fonin, A. V.; Sulatskaya, A. I.; Kuznetsova, I. M.; Turoverov, K. K., Fluorescence of dyes in solutions with high absorbance. Inner filter effect correction. *PLoS One* **2014,** *9* (7), e103878.

Chapter 2: Freeze-Thaw Stability of NETs at -20°C

Abstract

Red blood cell (RBC)-derived carriers are an emerging technology for delivery of biomedical cargoes. In particular, the near-infrared (NIR) dye, indocyanine green, can be loaded into RBC-derived carriers for biomedical imaging applications. We refer to these constructs as NIR erythrocyte-mimicking transducers (NETs). To facilitate the transport and long-term storage of NETs, we investigated frozen storage at -20°C as a method for preserving nano-sized NETs formed by mechanical extrusion (nNETs). Upon freeze-thawing, we determined that the optical properties, and zeta potential of nNETs remained unaffected by frozen storage for up to eight weeks. We also determined that their in-vitro uptake in SKOV3 cancer cells and in-vivo biodistribution in Swiss Webster mice remained unchanged. Therefore, freezing at -20°C may be a potential method for long-term storage and rapid deployment of nNETs in a clinical setting.

2.1 Introduction

Use of red blood cell (RBC) membranes as carrier vehicles is being widely studied as a means of delivering cargo to relevant biomedical targets. These cargos can range from drugs and biologics,[1-4] as well as optical and magnetic resonance contrast agents.[5-6] We are interested in using erythrocyte-derived carriers for intravenous delivery of the near-infrared (NIR) fluorophore, indocyanine green (ICG) for biomedical fluorescence imaging and phototherapy.[7-8] ICG enjoys several advantages as an exogenous contrast agent, including FDA approval for assessment of heart and liver function, and clinical usage in other procedures, including sentinel lymph node biopsy,[9-12] retinal angiography,[13-16] and

fluorescence-guided surgery.[17-19] Therefore, we have encapsulated ICG within nano-sized erythrocyte-derived carriers, and hereon refer to them as NIR erythrocyte-mimicking transducers (NETs).[20]

Low temperature storage of a biological material, such as NETs, can be used to reduce the rate of biological degradation processes acting on the material.[21] Therefore, we investigated the feasibility of storing NETs at -20°C as a means for preserving them during transport and enabling long-term storage. Previously, we determined that micron-sized and nano-sized NETs (μNETs and nNETs, respectively) formed by extrusion had stable NIR fluorescence for up to 12 hours at 37°C and 4°C storage conditions, which mimic those found in both the body and a standard laboratory refrigerator, respectively.[22]

Previous work by Kuo et al indicated that the diameters of nano-sized erythrocyte ghosts (nEGs) formed by extrusion had were unaffected by up to five freeze-thaw cycles.[23] However, that study did not investigate the influence of storage time on size, zeta potential, or on the encapsulated cargo. Therefore, we sought to observe the effects of -20°C frozen storage on the efficacy of nNETs. The -20°C storage condition is available at most medical clinics, and requires only a common refrigerator.

We studied the effects of -20°C freezing on the optical and physical properties of nano-sized NETs (nNETs). We saw no appreciable changes in their size, zeta potential, or their absorbance and fluorescence spectra. We then tested the *in-vitro* uptake of frozen-thawed nNETs by SKOV3 ovarian cancer cells, and their *in-vivo* biodistribution in mice. For both the *in-vitro* and *in-vivo* studies, we found there to be no statistically significant differences between frozen-thawed and freshly prepared nNETs.

2.2 Results and Discussion

2.2.1 Absorption characteristics of frozen-thawed particles

The absorption characteristics of NETs can indicate if there was any lysis or ICG leakage as a result of frozen storage. For intact RBCs (**Figure 2.1a**) a single freeze-thaw cycle was accompanied by a large drop in scattering-induced light attenuation across the entire visible spectrum. This can be attributed to lysis of the RBCs upon freeze-thawing.[24-25] The absorption spectra of frozen-thawed RBCs indicated the continued presence of hemoglobin as indicated by characteristics peaks for oxyhemoglobin near 550 nm[26], as well as a strong Soret band near 400 nm.[27]

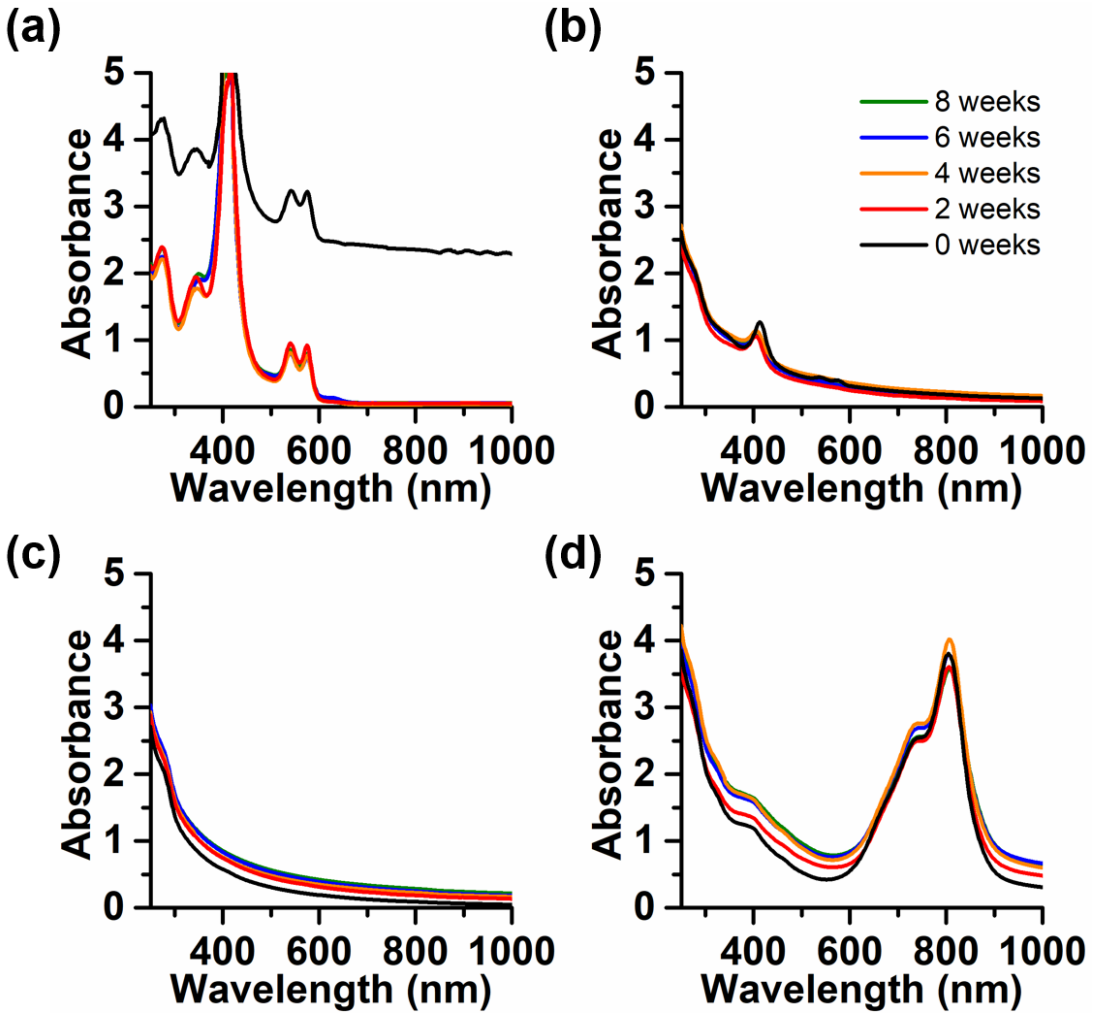

Figure 7. Absorbance spectra of frozen-thawed (a) RBCs, (b) nRBCs, (c) nEGs, and (d) nNETs after storage for up to eight weeks at -20°C.

Nano-extruded RBCs (nRBCs) appeared to preserve their original absorption spectra after frozen storage for up to eight weeks (**Figure 1b**), and continued to show the characteristic peaks for the Soret band, and oxyhemoglobin. This may be due to their small size being less susceptible to damage by the formation of ice crystals. nEGs (**Figure 1c**), and nNETs (**Figure 1d**) also did not show the characteristic drop in scattering that RBCs did, suggesting that their small size prevented further lysis upon freeze-thawing. nNETs

also did not show any appreciable decrease in NIR absorption, indicating that there was minimal ICG leakage from the nNETs in response to freeze-thawing.

2.2.2 Fluorescence characteristics of frozen-thawed particles

The NIR fluorescence emission spectra of each formulation was directly correlated with ICG content. Since RBCs did not contain any ICG, their emission spectra did not show any signal, regardless of their lysis (**Figure 2a**). The same trend was observed for nRBCs (**Figure 2b**), and nEGs (**Figure 2c**).

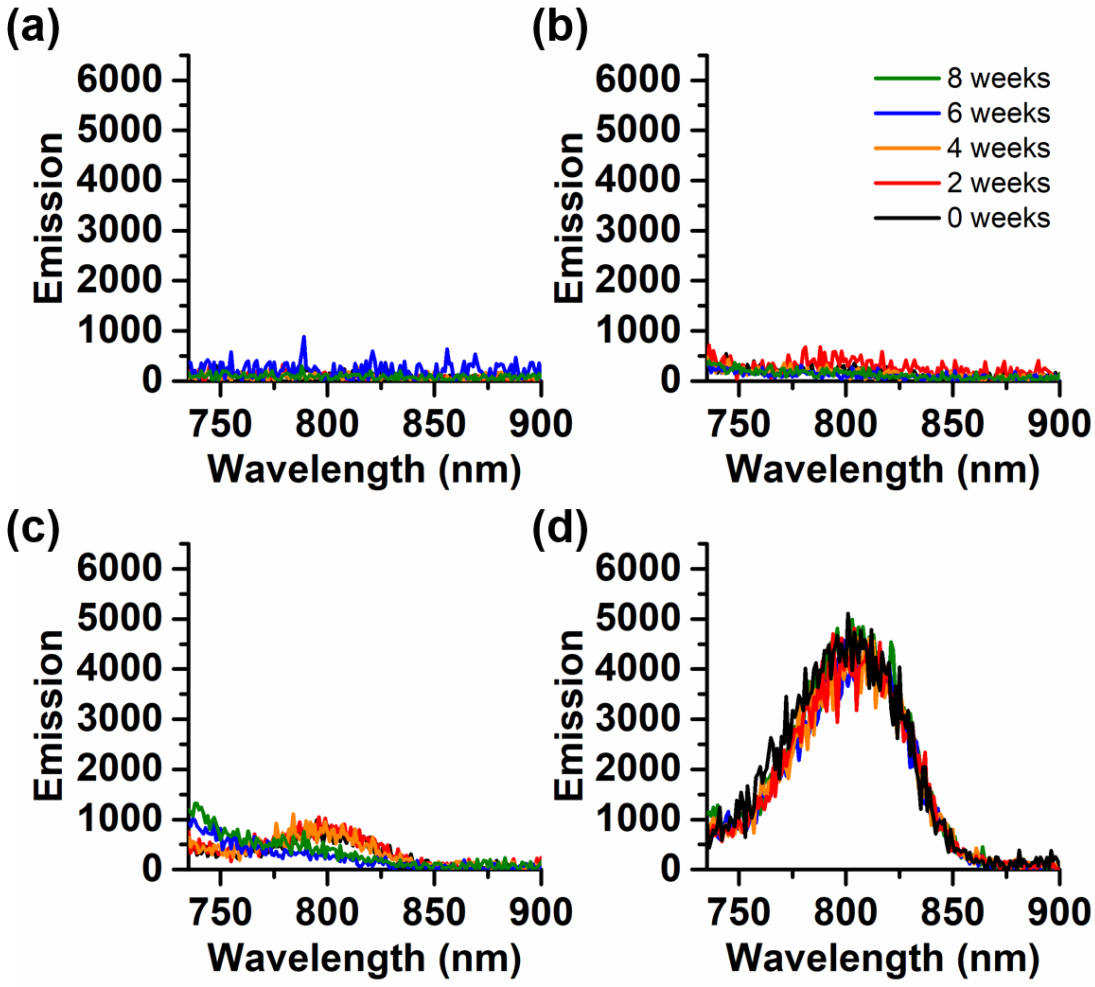

Figure 8. Fluorescence emission (excitation wavelength: 720 nm) of (a) RBCs, (b) nRBCs, (c), nEGs, and (d) nNETs after storage for up to eight weeks at -20°C.

For nNETs (**Figure 2d**), there was noticible NIR fluorescence peak centered near 800 nm. The fluorescence of nNETs remained constant as a function of storage time at -20°C (up to eight weeks). This indicated that the fluorescence of ICG within the constructs was not affected by freeze-thaw cycling, and also provided further evidence suggesting that ICG did not leak from the particles upon thawing after -20°C frozen storage.

2.2.3 Size and zeta potential of frozen-thawed particles

RBCs and micron-sized EGs (μEGs) showed a dramatic reduction in z-average diameter in response to a single freeze-thaw cycle (**Figure 3a**), which supports the reduction in scattering presented in **Figure 1a**. This result was expected, since freeze-thawing is already known to disrupt and lyse mammalian cells.[24-25] We attribute this to the fact that the grain size for ice crystals in frozen biological samples is on the order of tens-of-micrometers, which can easily trap and disrupt the membranes of RBCs and μEGs at the grain boundaries.[28-29] Prevention of freeze-thaw lysis of micron-sized EGs, RBCs has previously been achieved by addition of cryoprotectants, such as glycerol, dimethyl sulfoxide, or other crystallization inhibitors.[30-31]

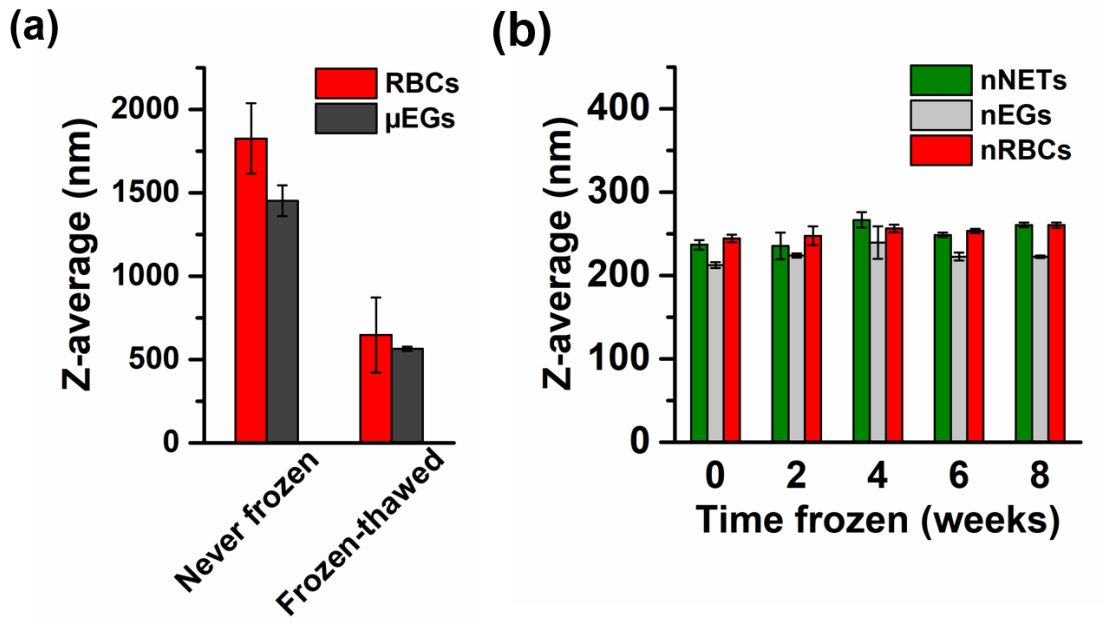

Figure 9. Hydrodynamic diameter (z-average) of (a) RBCs and micron-sized before and after one freeze-thaw cycle, and (b) nano-sized formulations

Nano-sized particles, nNETs, nEGs, and nRBCs did not suffer from lysis upon freeze-thawing out to eight weeks. The initial Z-average diameter of nNETs was 237 ± 6 nm, and was not statistically different from nRBCs at all time points. The Z-average diameters of nNETs were slightly larger than that of nEGs, due to intercalation of ICG within the membrane bilayer of nNETs.[22, 32] The diameters of nRBCs, nNETs, and nEGs remained stable after frozen storage at -20°C for up to eight weeks. We attribute the size-stability of these nano-sized particles to the fact that a large number of nanoparticles can fit within a single grain of an ice crystal, and so only a relatively small number of nanoparticles will be trapped and disrupted at the grain boundary.

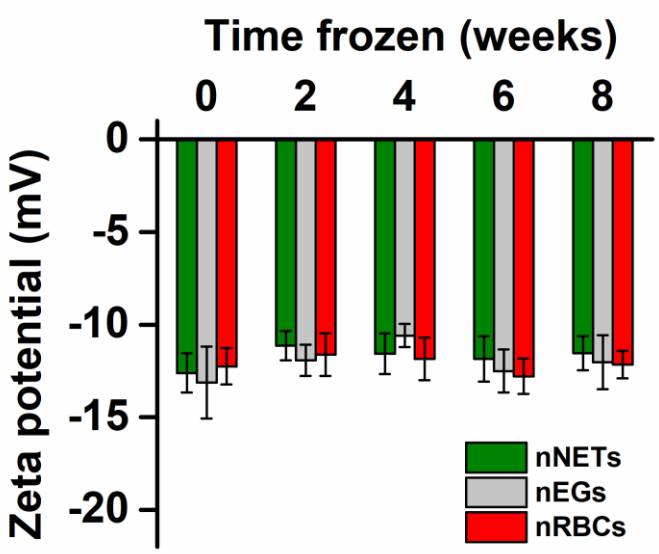

Figure 10. Zeta potential of nano-sized formulations compared to native RBCs.

We also measured the zeta potential (ζ) of nano-sized formulations compared to that of unfrozen bovine RBCs (**Figure 10**). The initial ζ of nEGs, nRBCs, and nNETs were not statistically different from that of fresh RBCs (-12.1 ± 1.0 mV). The ζ of these nano-sized formulations also remained constant after eight weeks of frozen storage, and after eight weeks were not statistically different from their initial values ($p > 0.05$).

2.2.4 In-vitro uptake of nNETs and frozen-thawed in SKOV3 ovarian cancer cells

We did not detect any statistical differences in NIR fluorescence emission of SKOV3 ovarian cancer cells that were incubated for two hours with frozen, or non-frozen nNETs (**Figure 11**, $p = 0.47$). Frozen-thawed nNETs and nNETs were then tested in SKOV3 ovarian cancer cells to assess any differences in uptake due to freeze-thaw cycling.

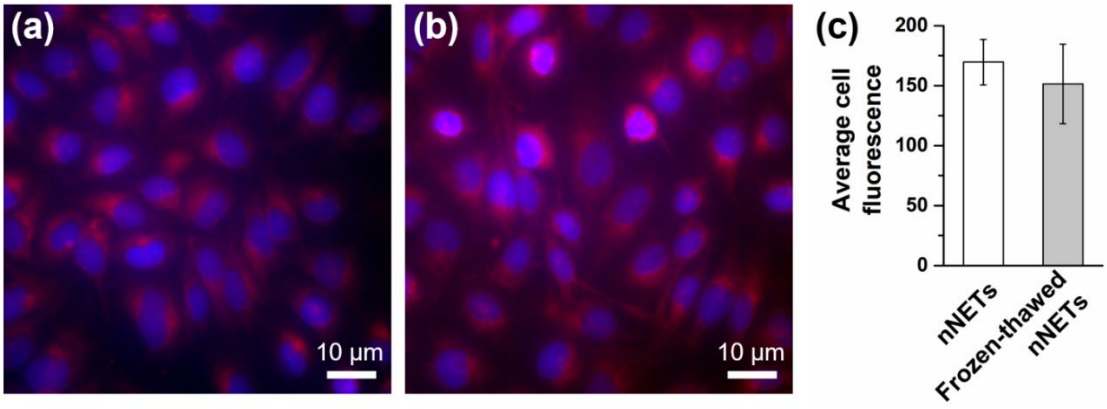

Figure 11. Ovarian cancer cells (SKOV3) that were incubated with (a) nNETs and (b) frozen-thawed nNETs for two hours at 37°C. (c) Quantification of average cell intensity no statistical differences due to freeze-thawing of particles (n = 3).

2.2.5 In-vivo biodistribution of nNETs and frozen-thawed nNETs in Swiss Webster mice

The formulations were then injected via tail vein into Swiss Webster mice to assess any differences in biodistribution for nNETs and frozen-thawed nNETs. Eighteen hours post-injection, the mice were sacrificed and their organs were weighed, then homogenized in 5% sodium dodecyl sulfate. The fluorescence spectra of organ homogenates were taken immediately afterwards to minimize degradation of ICG in the aqueous SDS.[33]

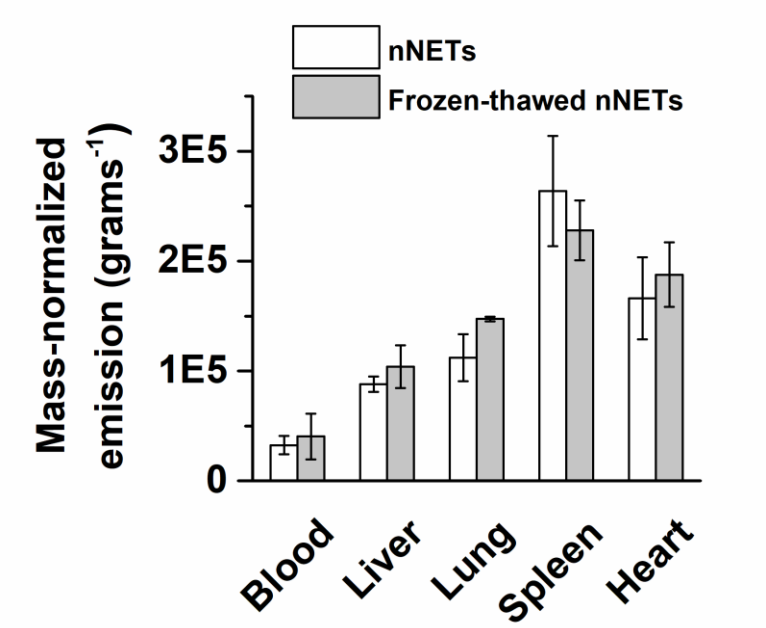

Figure 12. Biodistribution of NIR fluorescence emission in homogenized mouse tissues 18 hours after injection of nNETs and frozen-thawed nNETs [$n = 3$, see Equation (6)].

Using a two-way analysis of variants (ANOVA), there were no statistically significant differences in NIR fluorescence emission for homogenized mice organs that originated from either mice injected with nNETs or frozen-thawed nNETs (**Figure 12**, $p = 0.36$). We also found no statistical interaction between freezing and the amount of NIR signal detected from each organ ($p = 0.22$). Thus, there were no apparent differences in biodistribution for freeze-thawing of nNETs.

2.3 Conclusion

Frozen storage of nNETs at -20°C did not appear to cause ICG leakage due to no observable differences in their optical absorption, NIR fluorescence emission, hydrodynamic diameter, and zeta potential of nNETs after up to eight weeks of frozen storage. Micron-sized particles, including RBCs, and μEGs.

2.4 Experimental

2.4.1 Fabrication of nano-sized RBC-derived particles

μEGs were fabricated by hypotonic depletion of human RBCs, and used for freeze-thaw experiments. In brief, RBCs were washed in cold 1X PBS (5 min, 800 × g), then washed in 0.25X PBS (20 min, 20,000 × g) repeatedly until the supernatant ran clear. The resulting μEGs were then re-suspended in 1X phosphate-buffered saline (PBS), centrifuged for 20 min, 20,000 × g once more, and re-suspended in the same volume as the RBCs used to create them.

The μEGs were then diluted 1:10 in 1X PBS and serially extruded through polycarbonate membranes with track-etched pore sizes of 800, 400, and 200 nm (Whatman®, GE Healthcare) using nitrogen gas pressure in a 10 ml Lipex® extruder (Transferra Nanosciences). The samples were passed through each pore size at least three times before reducing the pore size to the next smaller pore diameter. The resulting nEGs were then loaded with ICG in a 1:1:1 volume ratio with Sørensen buffer and 75 μM ICG (final ICG loading concentration was 25 μM). RBCs were also extruded using the above extrusion procedure to form nano-sized RBCs (nRBCs).

2.4.2 Freeze-thawing of RBC-derived particle formulations

Particle formulations were stored at -20°C overnight to allow for complete freezing, then incubated up to eight weeks before thawing and subsequent analysis. Frozen aliquots were thawed at room temperature and characterized. For characterization, we measured their optical absorbance, fluorescence emission, hydrodynamic size, and zeta potential, similar to our previous work.[22]

2.4.3 Absorption characterization of frozen-thawed RBC-derived particles

We measured the steady-state absorption spectra of each formulation before and after frozen storage using a JASCO V-670 UV-vis spectrophotometer (Tokyo, Japan) in transmission mode with a quartz absorbance microcuvette (1 cm pathlength). The spectral range for all absorbance measurements was from 230-1100 nm to ensure that both the UV and NIR absorption, from proteins and ICG respectively, were recorded.

2.4.4 Fluorescence characterization of frozen-thawed RBC-derived particles

The fluorescence emission of RBC-derived particle formulations was measured before and after frozen storage, we collected their emission spectra using a Horiba Jobin Yvon FluoroLog 3 (Kyoto, Japan) and a quartz fluorescence microcuvette (Starna Cells, Atascadero, CA). The excitation wavelength was 720 nm, and the emission was collected from 735 – 900 nm.

2.4.5 DLS measurement of RBC-derived particle diameters and zeta potentials

We measured the size and zeta potential of RBC-derived particle formulations using a Malvern Zetasizer NanoZS (Malvern, United Kingdom). Samples were suspended in 1 ml 1X PBS within disposable polystyrene cuvettes (1 cm pathlength). Each DLS measurement was collected at 90° scattering angle. Each sample was measured eight times, and the average and standard deviation (SD) of these measurements were reported.

Zeta potentials (ζ) were also measured by DLS using the Smoluchowski approximation. Each measurement was done in a folded capillary cell at 22 °C. Similar to the z-average diameter measurements, the ζ of each formulation of NETs was measured eight times, and the average and SD was reported.

2.4.6 Assessment of biodistribution of nNETs and frozen-thawed nNETs in Swiss Webster mice

The biodistribution of NIR signal was assessed after administering ≈100 µl of either nNETs or frozen-thawed nNETs into female Swiss Webster mice (n = 3 for each formulation) via tail-vein injection under isoflurane anesthesia. All animal maintenance and experimental procedures were performed in accordance with the Public Health Service Policy, U.S. Department of Agriculture, (USDA), and the American Veterinary Medical Association (AVMA).[8] The animal study was approved by the University of California, Riverside, Institutional Animal Care and Use Committee (IACUC). Eighteen hours post-injection, the mice were sacrificed by CO_2 asphyxiation and a sample of blood was immediately drawn via cardiac puncture. The organs were then harvested for analysis by fluorescence spectroscopy.

The organs were weighed, then incubated in 1 ml 5% SDS for 30 mins before being homogenized using an Omni Tissue Homogenizer. After homogenization, an additional 4 ml of 5% SDS was added, and the homogenized organs were then incubated for 30 min to allow the release of ICG from cells. The homogenate was centrifuged for 45 min at to remove the solids, and the fluorescence spectra of the supernatants were measured in response to 720 nm excitation.

We integrated the emission spectra and divided this quantity by the mass of the organ measured to define the quantity I^*.

$$I^* = \frac{\int_{735\ nm}^{900\ nm} f(\lambda_{em}) d\lambda_{em}}{m_{organ}} \qquad (6)$$

where $f(\lambda_{em})$ is the fluorescence emission as a function of λ_{em}, the emission wavelength, and m_{organ} is the mass of the organ. From this we obtained a quantitative measure of the relative amount of NIR signal that was contained per gram of each organ.

2.5 References

1. Leuzzi, V.; Micheli, R.; D'Agnano, D.; Molinaro, A.; Venturi, T.; Plebani, A.; Soresina, A.; Marini, M.; Leali, P. F.; Quinti, I.; Pietrogrande, M. C.; Finocchi, A.; Fazzi, E.; Chessa, L.; Magnani, M., Positive effect of erythrocyte-delivered dexamethasone in ataxia-telangiectasia. *Neurol. Neuroimmunol. Neuroinflammation* **2015,** *2* (3).

2. Han, X.; Shen, S.; Fan, Q.; Chen, G.; Archibong, E.; Dotti, G.; Liu, Z.; Gu, Z.; Wang, C., Red blood cell-derived nanoerythrosome for antigen delivery with enhanced cancer immunotherapy. *Sci. Adv.* **2019,** *5* (10), eaaw6870.

3. Magnani, M.; Rossi, L.; Fraternale, A.; Bianchi, M.; Antonelli, A.; Crinelli, R.; Chiarantini, L., Erythrocyte-mediated delivery of drugs, peptides and modified oligonucleotides. *Gene Ther.* **2002,** *9* (11), 749-751.

4. Muzykantov, V. R., Drug delivery by red blood cells: vascular carriers designed by mother nature. *Expert Opin. Drug Delivery* **2010,** *7* (4), 403-427.

5. Markov, D. E.; Boeve, H.; Gleich, B.; Borgert, J.; Antonelli, A.; Sfara, C.; Magnani, M., Human erythrocytes as nanoparticle carriers for magnetic particle imaging. *Phys. Med. Biol.* **2010,** *55* (21), 6461-6473.

6. Johnson, K. M.; Tao, J. Z.; Kennan, R. P.; Gore, J. C., Gadolinium-bearing red cells as blood pool MRI contrast agents. *Magn. Reson. Med.* **1998,** *40* (1), 133-142.

7. Burns, J. M.; Vankayala, R.; Mac, J. T.; Anvari, B., Erythrocyte-derived theranostic nanoplatforms for near infrared fluorescence imaging and photodestruction of tumors. *ACS Appl. Mater. Interfaces* **2018,** *10* (33), 27621-27630.

8. Vankayala, R.; Corber, S. R.; Mac, J. T.; Rao, M. P.; Shafie, M.; Anvari, B., Erythrocyte-derived nanoparticles as a theranostic agent for near-infrared fluorescence imaging and thrombolysis of blood clots. *Macromol. Biosci.* **2018**, 1700379.

9. Zhang, X.; Li, Y.; Zhou, Y.; Mao, F.; Lin, Y.; Guan, J.; Sun, Q., Diagnostic performance of indocyanine green-guided sentinel lymph node biopsy in breast cancer: a meta-analysis. *PLoS One* **2016,** *11* (6), e0155597.

10. Pitsinis, V.; Provenzano, E.; Kaklamanis, L.; Wishart, G. C.; Benson, J. R., Indocyanine green fluorescence mapping for sentinel lymph node biopsy in early breast cancer. *Surg. Oncol.* **2015,** *24* (4), 375-379.

11. Namikawa, K.; Yamazaki, N., Sentinel lymph node biopsy guided by indocyanine green fluorescence for cutaneous melanoma. *Eur. J. Dermatol.* **2011,** *21* (2), 184-90.

12. Hayashi, T.; Furukawa, H.; Oyama, A.; Funayama, E.; Saito, A.; Yamao, T.; Yamamoto, Y., Sentinel lymph node biopsy using real-time fluorescence navigation with indocyanine green in cutaneous head and neck/lip mucosa melanomas. *Head Neck* **2012,** *34* (5), 758-61.

13. Baillif, S.; Wolff, B.; Paoli, V.; Gastaud, P.; Mauget-Faysse, M., Retinal fluorescein and indocyanine green angiography and spectral-domain optical coherence tomography findings in acute retinal pigment epitheliitis. *Retina* **2011,** *31* (6), 1156-63.

14. Bearelly, S.; Espinosa-Heidmann, D. G.; Cousins, S. W., The role of dynamic indocyanine green angiography in the diagnosis and treatment of retinal angiomatous proliferation. *Br. J. Ophthalmol.* **2008,** *92* (2), 191-6.

15. Cohen, S. M., Indocyanine green angiography of a laser-induced retinal-choroidal venous anastomosis. *Ophthalmic Surg. Lasers* **1997,** *28* (1), 65-6.

16. Wolf, S.; Remky, A.; Elsner, A. E.; Arend, O.; Reim, M., Indocyanine green video angiography in patients with age-related maculopathy-related retinal pigment epithelial detachments. *Ger. J. Ophthalmol.* **1994,** *3* (4-5), 224-7.

17. Cacciamani, G. E.; Shakir, A.; Tafuri, A.; Gill, K.; Han, J.; Ahmadi, N.; Hueber, P. A.; Gallucci, M.; Simone, G.; Campi, R.; Vignolini, G.; Huang, W. C.; Taylor, J.; Becher, E.; Van Leeuwen, F. W. B.; Van Der Poel, H. G.; Velet, L. P.; Hemal, A. K.; Breda, A.; Autorino, R.; Sotelo, R.; Aron, M.; Desai, M. M.; De Castro Abreu, A. L., Best practices in near-infrared fluorescence imaging with indocyanine green (NIRF/ICG)-guided robotic urologic surgery: a systematic review-based expert consensus. *World J. Urol.* **2019**.

18. Namikawa, T.; Sato, T.; Hanazaki, K., Recent advances in near-infrared fluorescence-guided imaging surgery using indocyanine green. *Surg. Today* **2015,** *45* (12), 1467-74.

19. D. Souza, A. V.; Lin, H.; Henderson, E. R.; Samkoe, K. S.; Pogue, B. W., Review of fluorescence guided surgery systems: identification of key performance capabilities beyond indocyanine green imaging. *J. Biomed. Opt.* **2016,** *21* (8), 80901.

20. Bahmani, B.; Bacon, D.; Anvari, B., Erythrocyte-derived photo-theranostic agents: hybrid nano-vesicles containing indocyanine green for near infrared imaging and therapeutic applications. *Sci. Rep.* **2013,** *3*.

21. Fuhrman, G. J.; Fuhrman, F. A., Oxygen consumption of animals and tissues as a function of temperature. *J. Gen. Physiol.* **1959,** *42* (4), 715-722.

22. Tang, J. C.; Partono, A.; Anvari, B., Near-infrared-fluorescent erythrocyte-mimicking particles: physical and optical characteristics. *IEEE Trans. Biomed. Eng.* **2019,** *66* (4), 1034-1044.

23. Kuo, Y. C.; Wu, H. C.; Hoang, D.; Bentley, W. E.; D'Souza, W. D.; Raghavan, S. R., Colloidal properties of nanoerythrosomes derived from bovine red blood cells. *Langmuir* **2016,** *32* (1), 171-179.

24. Lovelock, J. E., The haemolysis of human red blood-cells by freezing and thawing. *Biochim. Biophys. Acta* **1953,** *10* (3), 414-426.

25. Shatzkes, K.; Teferedegne, B.; Murata, H., A simple, inexpensive method for preparing cell lysates suitable for downstream reverse transcription quantitative PCR. *Sci. Rep.* **2014,** *4*.

26. Horecker, B. L., The absorption spectra of hemoglobin and its derivatives in the visible and near infra-red regions. *J. Biol. Chem.* **1943,** *148* (1), 173-183.

27. Uppal, S.; Kumar, A.; Shandilya, M.; Mukhi, N.; Singh, A. K.; Kateriya, S.; Kaur, J.; Kundu, S., Penta- and hexa-coordinate ferric hemoglobins display distinct pH titration profiles measured by Soret peak shifts. *Anal. Biochem.* **2016,** *510*, 120-128.

28. van der Sman, R. G. M.; Voda, A.; van Dalen, G.; Duijster, A., Ice crystal interspacing in frozen foods. *J. Food Eng.* **2013,** *116* (2), 622-626.

29. van der Sman, R. G. M., Phase field simulations of ice crystal growth in sugar solutions. *Int. J. Heat Mass Transfer* **2016,** *95*, 153-161.

30. Lovelock, J. E.; Bishop, M. W. H., Prevention of freezing damage to living cells by dimethyl sulphoxide. *Nature* **1959,** *183* (4672), 1394-1395.

31. Deller, R. C.; Vatish, M.; Mitchell, D. A.; Gibson, M. I., Glycerol-free cryopreservation of red blood cells enabled by ice-recrystallization-inhibiting polymers. *ACS Biomater. Sci. Eng.* **2015,** *1* (9), 789-794.

32. Vankayala, R.; Mac, J. T.; Burns, J. M.; Dunn, E.; Carroll, S.; Bahena, E. M.; Patel, D. K.; Griffey, S.; Anvari, B., Biodistribution and toxicological evaluation of micron- and nano-sized erythrocyte-derived optical particles in healthy Swiss Webster mice. *Biomater. Sci.* **2019,** *7* (5), 2123-2133.

33. Saxena, V.; Sadoqi, M.; Shao, J., Degradation kinetics of indocyanine green in aqueous solution. *J. Pharmaceut. Sci.* **2003,** *92* (10), 2090-7.

Chapter 3: Prolonged Circulation of a Red Cell-Based NIR Fluorescence Contrast Agent via Membrane Cholesterol Enrichment

Abstract

Hypotonic loading is a widely used strategy for encapsulating therapeutic and/or diagnostic cargo into human red blood cells (RBCs). We demonstrate that encapsulation of the NIR fluorescent dye, indocyanine green, under traditional hypotonic loading conditions (~80 mOsm) results in the outward display of phosphatidylserine (PS), a known apoptotic marker, on the outer membrane leaflet. These ICG-loaded RBC carriers are hereon referred to as NIR erythrocyte-mimicking transducers (NETs). The outward display of PS on NETs can be mitigated by the enrichment of membrane cholesterol on these RBC carriers. We demonstrate that cholesterol-enriched NETs have reduced externalization of phosphatidylserine that is closer to that of native RBCs compared to NETs fabricated without cholesterol enrichment. The reduced PS expression on the surface of cholesterol-enriched NETs results in reduced uptake in RAW 264.7 macrophages and prolonged intravenous circulation in healthy Swiss Webster mice.

3.1 Introduction

Erythrosomes, a portmanteau of the words ‘erythrocyte’ and ‘liposome’, or erythrocyte ghosts (EGs), are red blood cell (RBC)-derived vesicles that can encapsulate a wide variety of biomedical diagnostic and therapeutic cargoes.[1-3] These include, but are not limited to: chemotherapeutic drugs, imaging contrast agents (CT, optical, and magnetic resonance), and photosensitizers.[3-5] Encapsulation of these agents within EGs can serve to extend the

circulation time of imaging contrast agents, and/or facilitate the prolonged release of therapeutic drugs.

Formation of EGs is typically done via hypotonic lysis and centrifugal washing of RBCs. We determined that this method inadvertently translocates the normally-internalized membrane lipid, phosphatidylserine (PS), to the outer leaflet of EGs. Normally, RBCs and other mammalian cells, confine PS to the inner cytosolic leaflet, while displaying phosphatidylcholine and sphingomyelin on the outer extracellular leaflet.[6-8] This membrane leaflet asymmetry is actively maintained by aminophospholipid translocases, which depend on the concentrations of divalent cations (Mg^{2+} and Ca^{2+}) and ATP.[8-10]

Externalization of PS to the outer membrane leaflet is a known indicator of apoptosis, and can result in the uptake of drug-loaded erythrosomes by Kupffer cells and splenic macrophages.[11-14]. PS-mediated phagocytosis is then followed by secretion of anti-inflammatory cytokines such as interleukin 10, and transforming growth factor-β, which may explain the quiet, non-inflammatory nature of apoptotic cell removal.[15-17] PS is also implicated in coagulation and may enhance endothelial uptake, though its effects on vascular biology remain to be investigated.[17]

We encapsulate the near-infrared (NIR) dye, indocyanine green (ICG), within erythrosomes due to its long-established clinical utility as a non-toxic biocompatible fluorescence contrast agent with international regulatory approval.[18-19] Encapsulation of ICG within erythrosomes can serve to prolong the notoriously short circulation time of ICG.[19-21] Thus, we are interested in these NIR erythrocyte-mimicking transducers (NETs)

due to their potential for use in biomedical fluorescence imaging and photo-activated treatment of tissue malformations.[22] We previously functionalized NETs with surface moieties for specific targeting capabilities, and have previously demonstrated the feasibility of micron-sized NETs (μNETs) for use in photothermal and photodynamic treatment of port wine stain, while nano-sized NETs (nNETs) can potentially be effective for targeting tumors, respectively.[23-25]

A growing number of commercial imaging systems, intended for real-time intraoperative fluorescence imaging, are being developed around ICG excitation and emission, many of which have been used in clinical surgery.[26-29] For future clinical translation, NETs may be fabricated in large-scale sterile conditions using fully-automated instruments.[30]

We discovered that the hypotonic lysis conditions used to fabricate previous formulations of NETs resulted in the externalization of PS onto the outer leaflet.[10] PS-exposed NETs may be used to deliver cargos to spleen, liver, and/or tumor-associated macrophages, but this would necessarily limit their circulation half-life in the vasculature.

Therefore, we developed a method for maintaining the confinement of PS to the inner cytosolic leaflet of μNETs and nNETs by enriching their plasma membranes with cholesterol.[31] Recent findings indicate that in healthy cells with low intracellular Ca^{2+} concentrations, PS exposure is prevented by membrane cholesterol-mediated suppression of phospholipid scramblase 1 (PLSCR 1), a protein that is responsible for the flopping of PS to the outer leaflet.[9] To enrich the membranes of micron-sized and nano-sized NETs (μNETs and nNETs respectively) with cholesterol, we complexed cholesterol with methyl-

β-cyclodextrin (MβCD), a small molecule that can facilitate insertion of cholesterol into the phospholipid bilayer.[32]

Herein, we investigate the effects of enriching the membrane cholesterol of NETs at different stages of the fabrication process, and demonstrate that cholesterol-enriched μNETs and nNETs indeed display less PS on their outer leaflets. Our in-vitro results indicate that cholesterol-enriched NETs show reduced phagocytic uptake by RAW 264.7 macrophages. Upon injection in vivo, cholesterol-enriched μNETs also exhibit prolonged circulation in the bloodstreams of healthy Swiss Webster mice.

3.2 Results and Discussion

3.2.1 Cholesterol-enrichment of μNETs and nNETs

Cholesterol-enriched μNETs and nNETs were prepared as detailed in the schematic diagram in **Figure 13a**. Cholesterol was inserted using the carrier molecule, methyl-β-cyclodextrin (MβCD). Two types of cholesterol-enriched μNETs were fabricated, denoted as c+μNETs and c+d+μNETs. The difference between the two is that c+μNETs is loaded with cholesterol only once after the erythrocyte ghost fabrication, whereas c+d+μNETs are loaded with cholesterol both during erythrocyte ghost fabrication, in addition to a second cholesterol-enrichment step immediately prior to loading ICG.

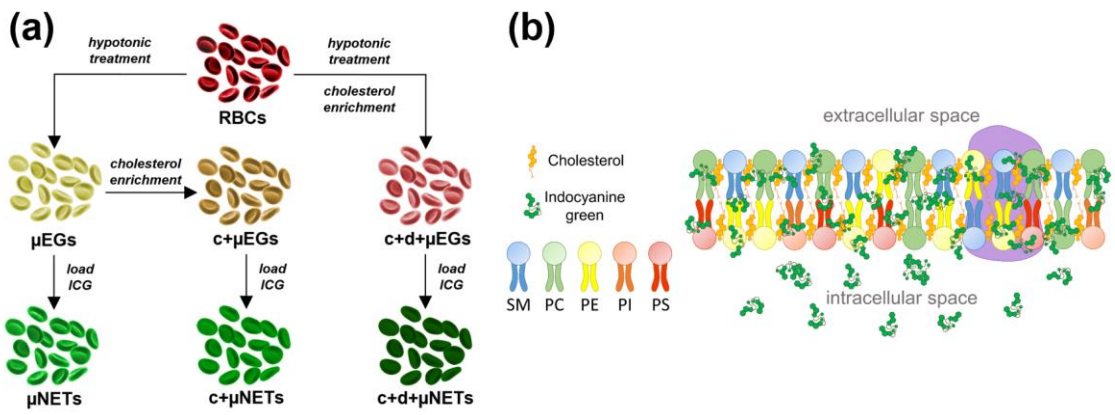

Figure 13. Illustrative diagram of the (a) top-down fabrication procedure for preparing cholesterol-enriched μNETs and, (b) membrane structure of cholesterol-enriched NETs (cytoskeleton not pictured). SM, sphingomyelin; PC, phosphatidylcholine; PE, phosphatidylethanolamine; PI, phosphatidylinositol; PS, phosphatidylserine.

A hypothetical cartoon of the membrane structure of cholesterol-enriched μNETs is presented as **Figure 13b**. Here we illustrate the intercalation of cholesterol in the membrane bilayer, and the native orientation of phospholipids in the RBC membrane.[33]

3.2.2 Morphology of cholesterol-enriched μNETs

Scattering data from flow cytometric analysis indicate that RBCs have the greatest FSC-A and SSC-A, while μNETs scatter the least in both forward and side scattering directions (**Figure 14a,b**). This trend arises as a result of the hypotonic treatment process that removes hemoglobin and other intracellular contents that can give rise to scattering.

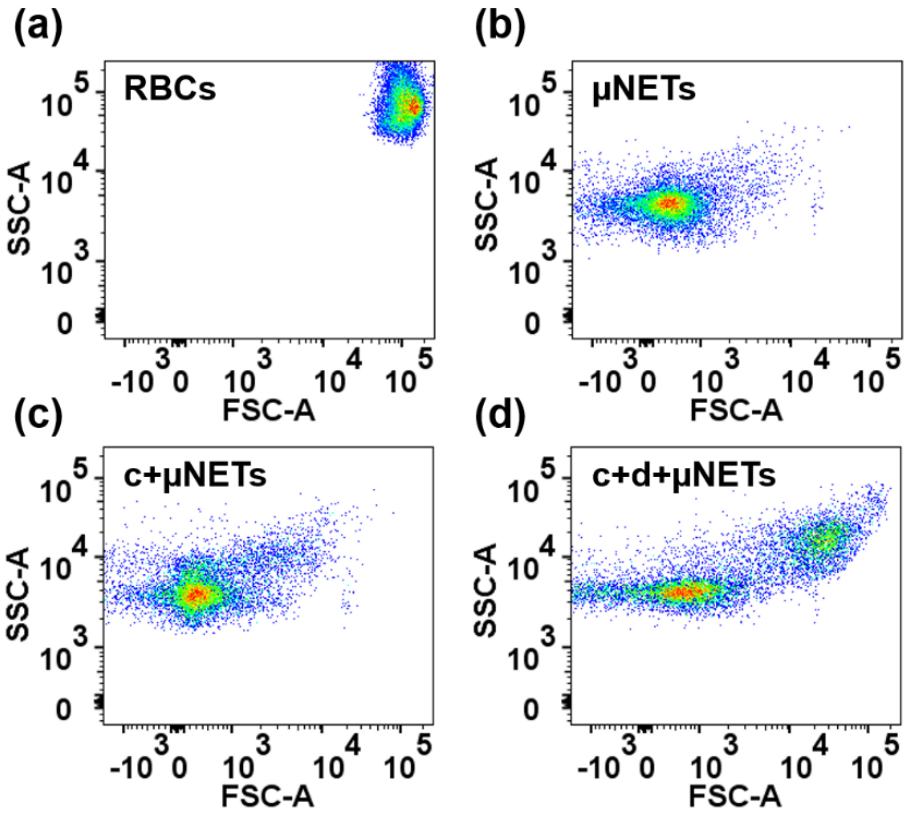

Figure 14. Representative forward vs side scattering analysis of (a) RBCs, (b) µNETs, (c) c+µNETs, and (d) c+d+µNETs. FSC-A and SSC-A refer to forward scattering area and side scattering area. Two distinct morphologies can be observed for c+d+µNETs.

Interestingly, c+µNETs and c+d+µNETs each had two distinct populations, one population that scattered like µNETs, and a second one closer to the RBC scattering region (**Figure 14c,d**). The second RBC-like populations found in samples of c+µNETs and c+d+µNETs can be attributed to particles that were only partially depleted of hemoglobin.

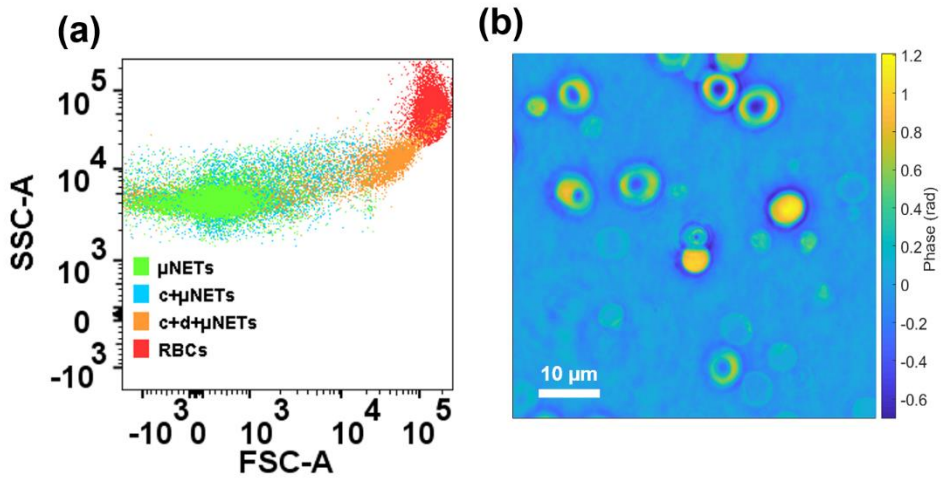

Figure 15. Morphological analysis of μNETs variants. (a) Combined dot plot of μNETs scattering. (b) Quantitative phase image of c+d+μNETs, which confirms the two subpopulations of RBC-like and μNET-like particles [see Equations (7) and (8)].

Using quantitative phase imaging, we confirmed the differences in scattering for cholesterol-enriched μNETs observed in **Figure 14** and **Figure 15a.** The optical phase delay of c+d+μNETs was found to be greater than that of c+μNETs, indicating that c+μNETs had less hemoglobin and/or other intracellular content (**Figure 15b**). Indeed, elevated levels of membrane cholesterol has been shown to stabilize and rigidify RBC membranes, which may explain the resistance to hemoglobin depletion during hypotonic treatment of cholesterol-enriched RBCs.[34-36] Since c+μNETs had lower overall cholesterol content than c+d+μNETs, the amount of hemolysis was greater for c+μNETs compared to c+d+μNETs.

3.2.3 Cholesterol enrichment reduces the expression of PS

Cholesterol enrichment throughout the hemoglobin depletion process resulted in c+d+μNETs that had statistically significantly higher membrane cholesterol compared to only one cholesterol enrichment step (c+μNETs) or no cholesterol enrichment at all (**Figure 16a**). Higher membrane cholesterol content correlated with reduced detection of PS on the particle surfaces, which we attribute to cholesterol-induced confinement of PS to the inner leaflet (**Figure 16b**).

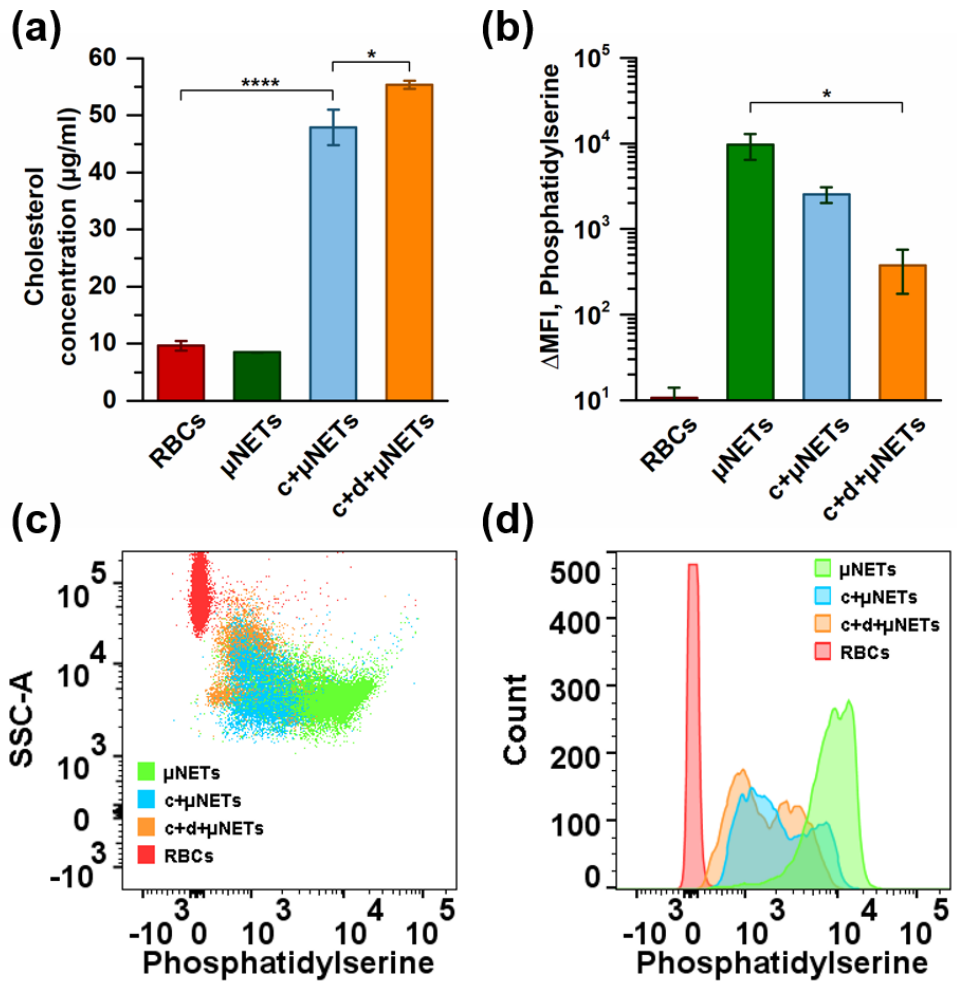

Figure 16. Characterization of the cholesterol content and externalized phosphatidylserine of µNETs. (a) Cholesterol concentration of RBCs, µNETs, and cholesterol-enriched µNETs (c+µNETs and c+d+µNETs). (b) Detection of externalized phosphatidylserine in µNETs variants. Asterisk brackets indicate statistically significant differences (*, $p < 0.05$; ****, $p < 0.0001$, n = 3). (c) Representative histograms of µNETs variants that were fluorescently labeled for PS using AV-AF488. (d) SSC-A vs PS labeling for µNETs variants, indicating that high SSC-A correlated with reduced externalization of PS on the outer leaflet.

We also noticed bimodal distributions of MFI for AV-AF488-labeled c+µNETs and c+d+µNETs, which confirmed that the two subpopulations with different scattering profiles in (**Figure 14c,d**) also had different levels of PS externalization (**Figure 16c**).

Particles that were more RBC-like (higher FSC-A and SSC-A) tended to have lower PS expression than those that were more ghost-like (**Figure 16d**).

3.2.4 Chol.-enriched µNETs show reduced uptake in RAW 264.7 macrophages

We investigated the effect of cholesterol enrichment on phagocytic uptake of µNETs by RAW 264.7 murine macrophages. The reduced externalization of PS in cholesterol-enriched c+µNETs resulted in lower uptake compared to unenriched µNETs (**Figure 17a**). The greater degree of cholesterol enrichment in c+d+µNETs resulted in further reduction in phagocytic uptake when compared to c+µNETs and µNETs (**Figure 17b)**.

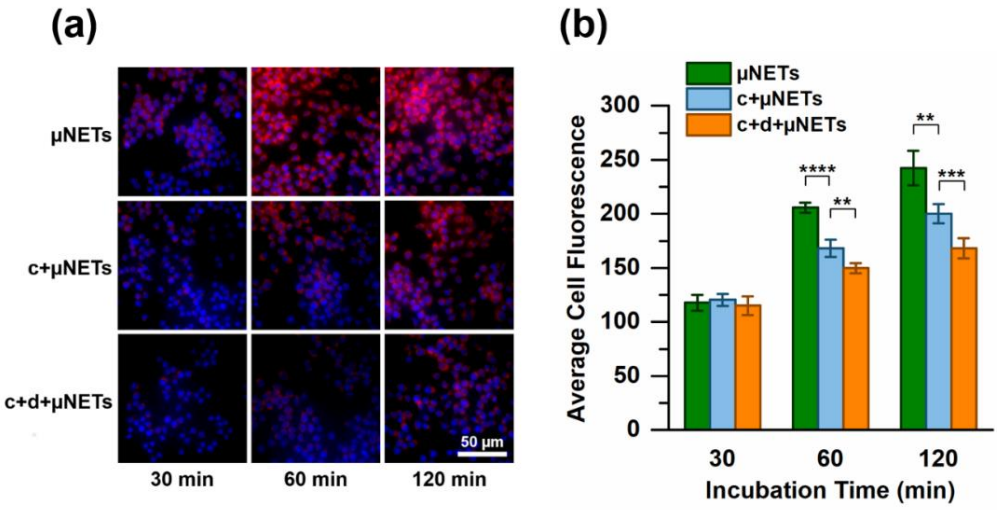

Figure 17. (a) In-vitro uptake assay of cholesterol-enriched µNETs by RAW 264.7 macrophages at 30, 60, and 120 minutes. (b) average fluorescence of RAW264.7 cells that were incubated with cholesterol-enriched µNET variants. Statistical significance is denoted using asterisk bars: single-asterisk denotes $p < 0.05$ and triple-asterisk denotes $p < 0.001$.

For 30 minute incubations, all formulations showed similarly low uptake. However, as the particle formulations were incubated for longer durations (60, 120 mins), µNETs were uptaken rapidly between 30 min and 1 hour, whereas c+µNETs and c+d+µNETs showed reduced uptake compared to µNETs at all time points.

3.2.5 Chol. µNETs show prolonged circulation in Swiss Webster mice

We compared the circulation kinetics of c+µNETs and c+d+µNETs with that of µNETs and free ICG (75 µM) in a skinfold dorsal window chamber model using Swiss Webster mice (**Figure 18a, b**). The baseline circulation half-life of 75 µM free ICG was 3.8 minutes.

We found that encapsulation within µNETs extended the circulation half-life to 8.5 ± 2.3 minutes. Surprisingly, c+µNETs had the nearly the same circulation time as µNETs (8.5 ± 2.9), while c+d+µNETs continued to extend the circulation half-life to 12.1 ± 3.8 minutes, as expected. However, the difference in circulation half-life between µNETs and c+d+µNETs was not statistically significant ($p > 0.05$). Assuming that the mean and standard deviations of the measured circulation half-life remained the same, we would need a sample size of eight ($n = 8$) for µNETs and c+d+µNETs to demonstrate statistical significance ($p < 0.05$).

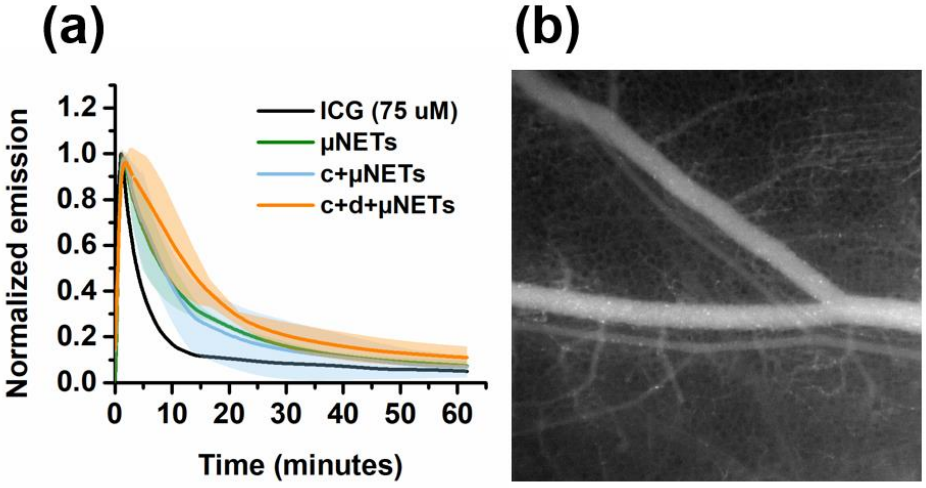

Figure 18. In-vivo circulation kinetics using mouse dorsal skinfold microvascular window chamber model. (a) Normalized intensity of main blood vessel over time in response to retro-orbital injection of µNETs, c+µNETs, and c+d+µNETs (n = 3). Free ICG (75 µM) is included as the black trace. (b) Representative NIR fluorescence image of c+µNETs circulating in a window chamber in vivo.

While cholesterol enrichment can reduce the amount of surface-exposed PS on μNETs, the literature suggests that cholesterol enrichment may reduce the overall deformability of μNETs. While our own preliminary measurements of μNET tensile stiffness (via optical tweezing methods, data not shown) indicate that cholesterol-enrichment can reduce the mechanical stiffness, this should not be interpreted as more deformable. In the context of in-vivo circulation and splenic clearance, the relevant stiffness is likely to be compressive, rather than tensile. Another important point is that the overall deformability of RBCs in the vasculature is largely due to the membrane viscosity, which is indeed affected by membrane cholesterol content.[37] Overall, cholesterol enrichment may result in lower *stiffness* due to modulation of the underlying membrane-cytoskeleton interaction, but would also result in higher *membrane viscosity* and bending modulus, which has been demonstrated to impede the passage of RBCs through tight microfluidic channels.[38]

3.2.6 Consideration for applying cholesterol-enrichment to nNETs

PS confinement via membrane cholesterol enrichment may benefit nano-sized NETs (nNETs) more than μNETs, because their smaller diameter reduces the importance of deformability for passage through the spleen. In other words, the potential drawback of reduced deformability for cholesterol-enriched nNETs is mitigated by their inherently small size. Indeed, there is a need for PS confinement for nano-sized formulations, since both mechanical extrusion and sonication methods will necessarily exposes PS on the membrane surface, even when using healthy PS-confined RBCs as the material precursor. Therefore, cholesterol-enrichment can be considered a viable method for confining PS on nNETs.

3.3 Conclusion

Externalized phosphatidylserine, a known marker of RBC senescence, on the outer surface of NETs, and other RBC-derived carriers can result in enhanced phagocytic removal from the vasculature due to PS-mediated adhesion to endothelium. This feature of NETs can potentially be exploited to guide drug-loaded erythrosomes to vascular malformations, such as port wine stain or atherosclerotic lesions, or immune cell rich sites, such as tumors. We have demonstrated that PS exposure can also be suppressed by the enrichment of membrane cholesterol resulting in reduced phagocytic uptake in vitro, and prolonged in-vivo circulation. Therefore, cholesterol-enriched RBC carriers have potential to be used in applications that require long intravenous circulation, such as systemic drug release or immunospecific targeting of cancers.

3.4 Experimental

3.4.1 Fabrication of μNETs

Red blood cells were washed twice in 1X PBS and depleted of hemoglobin by repeated washing in hypotonic 0.25X PBS. The resulting erythrocyte ghosts (μEGs) were then doped with indocyanine green (ICG, MP Biochemicals) by adding equivalent volumes of 1X μEGs, 0.1 M Sørensen's buffer, and 300 μM ICG. In total, the ICG loading buffer contained 100 μM ICG, at a tonicity of 175 mOsm. After incubating in ICG loading buffer for 30 min at 4°C, the resulting μNETs were washed twice in 1X PBS.

3.4.2 Cholesterol enrichment of NETs

We modified the membrane cholesterol content of NETs by incubating them with cholesterol complexed with methyl-β-cyclodextrin (MβCD) (Millipore Sigma).[32] A

flowchart of three different fabrication methods for membrane cholesterol manipulation is presented as **Figure 14** above. Briefly, c+μNETs were prepared by incubating μEGs with 1X PBS containing 15 mM water-soluble cholesterol (Sigma) with equimolar MβCD at 37°C for 1 hour prior to loading with indocyanine green (ICG, MP Biochemicals), as described in the previous section. c+d+μNETs were fabricated by hypotonic treatment of washed RBCs in buffer (0.25X PBS, 80 mOsm, pH = 8) containing 15 mM cholesterol/MβCD throughout the Hb depletion process, followed by incubation at 37°C for 1 hour, then ICG loading.

3.4.3 Flow cytometric quantification of externalized PS on μNETs

We used annexin V-Alexa Fluor 488 (AV-AF488) as a detection reagent to quantify the amount of externalized PS on NETs samples.[39] Specifically, 0.5 μl of μNETs (1X) was added to 500 μl of 1X annexin binding buffer (ABB, final Ca^{2+} concentration was 2.5 mM) and one drop (~40 μl) of annexinV Alexa Fluor 488 Ready Flow conjugate (ThermoFisher Scientific). NETs were incubated with AV-AF488 for ~20 min at 22°C and were analyzed using a BD LSR II flow cytometer.

FC analysis of externalized PS on μNETs was performed by first gating particles that tested positive for ICG in APC-Cy7 channel (633 nm excitation laser, 780 ± 30 nm emission filter). We considered ICG-positive particles to be μNETs and their presence in the known FSC vs. SSC scattering regime confirmed this (**Figure 15**). We then determined the mean fluorescence intensity (MFI) in FITC channel of cholesterol-enriched/unenriched μNETs that were fluorescently labeled for PS using AV-AF488.

FC analysis of externalized PS on RBC was performed by first gating the proper FSC vs. SSC scattering regime, followed by determination of MFI in FITC channel of AV-AF488-stained RBCs.

3.4.4 Quantification of membrane cholesterol content

The membrane cholesterol content of control and cholesterol-manipulated μNETs was quantified using the Amplex® Red Cholesterol Assay Kit (Invitrogen Molecular Probes). Briefly, this colorimetric assay is based on the reaction of cholesterol with cholesterol oxidase to yield H_2O_2 which can reacts with Amplex® Red reagent to produce detectable fluorescence.

3.4.5 In-vitro assessment of NETs uptake in RAW 264.7 macrophages

RAW 264.7 macrophages grown to passage 11 and were seeded at a density of 100,000 cells per well in a 96-well tissue culture plate (Corning) and incubated for 24 hours at 37°C in 5% CO_2 atmosphere in 100 μl of Dulbecco's Modified Eagle's Medium supplemented with 10% fetal bovine serum and 1% penicillin/streptomycin. For assessment of NETs uptake, 50 μl sample was mixed with 100 μl of serum-free DMEM and was added to each well and incubated at 37°C with 5% CO_2 for 30, 60, and 120 minutes. At each timepoint, cells were washed with PBS and fixed with 4% paraformaldehyde, permeablized with 2% Tween 20, and stained with 300 nM DAPI for five minutes each. Macrophages were rinsed with 100 μl of sterile 1X PBS between fixing, permeablization, and DAPI staining operations and then rinsed twice more with 1X PBS prior to imaging.

3.4.6 Fluorescence microscopy of RAW 264.7 macrophages

RAW 264.7 macrophages that were treated with the above in-vitro uptake procedure were imaged using a Nikon Eclipse Ti inverted fluorescence microscope. NETs uptake was visualized using a NIR filter set that contained a 740 nm ± 18 nm excitation filter and a 780 nm long pass emission filter (41037 - Li-Cor IR800, Chroma Technology Corp.). Cell nuclei were visualized using a DAPI filter set (DAPI-5060B-NTE, Semrock Inc.). ImageJ was used to normalize the window/level of the ICG channel of each image, and to stack DAPI and ICG channels into a composite RGB image.

3.4.7 Quantification of average cell fluorescence using ImageJ

We calculated the average NIR emission per cell in each image by integrating all pixels in the NIR channel (excitation and emission optics detailed above) and dividing the total NIR emission by the number of cells. Mathematically, we can represent this as:

$$\bar{I}_{cell} = \frac{\sum_{x=1}^{512}\sum_{y=1}^{512} I(x,y)}{n} \qquad (7)$$

where $\bar{I}_{cell}$ is the average NIR emission per cell, $I(x,y)$ is the NIR emission intensity value at position (x,y) in the image, and n is the number of cells in the image. The number n was obtained by counting the number of cell nuclei in the DAPI channel using a macro in ImageJ.[40]

3.4.8 Quantitative phase imaging of cholesterol-enriched μNETs

Quantitative phase images were obtained using a custom interferometric imaging system.[41-42] A spatial light modulator (Hamamatsu LCOS-SLM X-10468) was used to shift the phase of the background light (unscattered) in π/2 increments relative to the light passing through the sample (μNETs). Recombining the phase-shifted background images

with the scattered light from μNETs results in four unique intensity maps, which we denote with the amount of phase shift applied to the background: I_0, $I_{\frac{\pi}{2}}$, I_π, and $I_{\frac{3\pi}{2}}$. The phase difference ($\Delta\varphi$) between sample and background was then calculated using the following equation:

$$\Delta\varphi = \tan^{-1}\left(\frac{I_0 - I_\pi}{I_{\frac{\pi}{2}} - I_{\frac{3\pi}{2}}}\right) \qquad (7)$$

This was then converted a quantitative phase map, where the phase delay of the sample (relative to background) was calculated as:

$$\varphi = \tan^{-1}\left(\frac{\beta \sin\Delta\varphi}{1 + \beta\cos\Delta\varphi}\right) \qquad (8)$$

where β is the ratio between the amplitude of scattered and unscattered light.

3.5 References

1. Pouliot, R.; Saint-Laurent, A.; Chypre, C.; Audet, R.; Vitte-Mony, I.; Gaudreault, R. C.; Auger, M., Spectroscopic characterization of nanoerythrosomes in the absence and presence of conjugated polyethyleneglycols: an FTIR and P-31-NMR study. *Biochim. Biophys. Acta, Biomembr.* **2002,** *1564* (2), 317-324.

2. Kuo, Y. C.; Wu, H. C.; Hoang, D.; Bentley, W. E.; D'Souza, W. D.; Raghavan, S. R., Colloidal properties of nanoerythrosomes derived from bovine red blood cells. *Langmuir* **2016,** *32* (1), 171-179.

3. Villa, C. H.; Anselmo, A. C.; Mitragotri, S.; Muzykantov, V., Red blood cells: Supercarriers for drugs, biologicals, and nanoparticles and inspiration for advanced delivery systems. *Adv. Drug Deliv. Rev.* **2016,** *106*, 88-103.

4. Sternberg, N.; Georgieva, R.; Duft, K.; Baumler, H., Surface-modified loaded human red blood cells for targeting and delivery of drugs. *J. Microencapsulation* **2012,** *29* (1), 9-20.

5. Aryal, S.; Nguyen, T. D. T.; Pitchaimani, A.; Shrestha, T. B.; Biller, D.; Troyer, D., Membrane fusion-mediated gold nanoplating of red blood cell: a bioengineered CT-contrast agent. *ACS Biomater. Sci. Eng.* **2017,** *3* (1), 36-41.

6. Verkleij, A. J.; Zwaal, R. F.; Roelofsen, B.; Comfurius, P.; Kastelijn, D.; van Deenen, L. L., The asymmetric distribution of phospholipids in the human red cell membrane. A combined study using phospholipases and freeze-etch electron microscopy. *Biochim. Biophys. Acta* **1973,** *323* (2), 178-93.

7. Gordesky, S. E.; Marinetti, G. V., Asymmetric arrangement of phospholipids in human erythrocyte-membrane. *Biochem. Biophys. Res. Commun.* **1973,** *50* (4), 1027-1031.

8. Connor, J.; Gillum, K.; Schroit, A. J., Maintenance of lipid asymmetry in red blood cells and ghosts: effect of divalent cations and serum albumin on the transbilayer distribution of phosphatidylserine. *Biochim. Biophys. Acta*

1990, *1025* (1), 82-6.

9. Arashiki, N.; Takakuwa, Y., Maintenance and regulation of asymmetric phospholipid distribution in human erythrocyte membranes: implications for erythrocyte functions. *Curr. Opin. Hematol.* **2017,** *24* (3), 167-172.

10. Schrier, S. L.; Zachowski, A.; Herve, P.; Kader, J. C.; Devaux, P. F., Transmembrane Redistribution of Phospholipids of the Human Red-Cell Membrane during Hypotonic Hemolysis. *Biochim. Biophys. Acta* **1992,** *1105* (1), 170-176.

11. Nagata, S.; Suzuki, J.; Segawa, K.; Fujii, T., Exposure of phosphatidylserine on the cell surface. *Cell Death Differ.* **2016,** *23* (6), 952-961.

12. Bratosin, D.; Mazurier, J.; Tissier, J. P.; Estaquier, J.; Huart, J. J.; Ameisen, J. C.; Aminoff, D.; Montreuil, J., Cellular and molecular mechanisms of senescent erythrocyte phagocytosis by macrophages. A review. *Biochimie*

1998, *80* (2), 173-95.

13. Lee, S. J.; Park, S. Y.; Jung, M. Y.; Bae, S. M.; Kim, I. S., Mechanism for phosphatidylserine-dependent erythrophagocytosis in mouse liver. *Blood* **2011,** *117* (19), 5215-5223.

14. Schroit, A. J.; Madsen, J. W.; Tanaka, Y., In vivo recognition and clearance of red blood cells containing phosphatidylserine in their plasma membranes. *J. Biol. Chem.* **1985,** *260* (8), 5131-8.

15. Huynh, M. L.; Fadok, V. A.; Henson, P. M., Phosphatidylserine-dependent ingestion of apoptotic cells promotes TGF-beta1 secretion and the resolution of inflammation. *J. Clin. Invest.* **2002,** *109* (1), 41-50.

16. Korns, D.; Frasch, S. C.; Fernandez-Boyanapalli, R.; Henson, P. M.; Bratton, D. L., Modulation of macrophage efferocytosis in inflammation. *Front. Immunol.* **2011,** *2*, 57.

17. Darabi, M.; Kontush, A., Phosphatidylserine in atherosclerosis. *Curr. Opin. Lipidol.* **2016,** *27* (4), 414-20.

18. Frangioni, J. V., In vivo near-infrared fluorescence imaging. *Curr. Opin. Chem. Biol.* **2003,** *7* (5), 626-634.

19. Alander, J. T.; Kaartinen, I.; Laakso, A.; Patila, T.; Spillmann, T.; Tuchin, V. V.; Venermo, M.; Valisuo, P., A review of indocyanine green fluorescent imaging in surgery. *Int. J. Biomed. Imaging* **2012,** *2012*, 940585.

20. Desmettre, T.; Devoisselle, J. M.; Mordon, S., Fluorescence properties and metabolic features of indocyanine green (ICG) as related to angiography. *Surv. Ophthalmol.* **2000,** *45* (1), 15-27.

21. Hwang, Y.; Yoon, H.; Choe, K.; Ahn, J.; Jung, J. H.; Park, J. H.; Kim, P., In vivo cellular-level real-time pharmacokinetic imaging of free-form and liposomal indocyanine green in liver. *Biomed. Opt. Express* **2017,** *8* (10), 4706-4716.

22. Bahmani, B.; Bacon, D.; Anvari, B., Erythrocyte-derived photo-theranostic agents: hybrid nano-vesicles containing indocyanine green for near infrared imaging and therapeutic applications. *Sci. Rep.* **2013,** *3*.

23. Mac, J. T.; Nunez, V.; Burns, J. M.; Guerrero, Y. A.; Vullev, V. I.; Anvari, B., Erythrocyte-derived nano-probes functionalized with antibodies for targeted near infrared fluorescence imaging of cancer cells. *Biomed. Opt. Express* **2016,** *7* (4), 1311-1322.

24. Burns, J. M.; Vankayala, R.; Mac, J. T.; Anvari, B., Erythrocyte-derived theranostic nanoplatforms for near infrared fluorescence imaging and photodestruction of tumors. *ACS Appl. Mater. Interfaces* **2018,** *10* (33), 27621-27630.

25. Burns, J. M.; Jia, W. C.; Nelson, J. S.; Majaron, B.; Anvari, B., Photothermal treatment of port-wine stains using erythrocyte-derived particles doped with indocyanine green: a theoretical study. *J. Biomed. Opt.* **2018,** *23* (12).

26. Kim, T.; O'Brien, C.; Choi, H. S.; Jeong, M. Y., Fluorescence molecular imaging systems for intraoperative image-guided surgery. *Appl. Spectrosc. Rev.* **2018,** *53* (2-4), 349-359.

27. D. Souza, A. V.; Lin, H.; Henderson, E. R.; Samkoe, K. S.; Pogue, B. W., Review of fluorescence guided surgery systems: identification of key performance capabilities beyond indocyanine green imaging. *J. Biomed. Opt.* **2016,** *21* (8), 80901.

28. Boni, L.; David, G.; Mangano, A.; Dionigi, G.; Rausei, S.; Spampatti, S.; Cassinotti, E.; Fingerhut, A., Clinical applications of indocyanine green (ICG) enhanced fluorescence in laparoscopic surgery. *Surg. Endoscopy* **2015,** *29* (7), 2046-2055.

29. Griffiths, M.; Chae, M. P.; Rozen, W. M., Indocyanine green-based fluorescent angiography in breast reconstruction. *Gland Surg.* **2016,** *5* (2), 133-49.

30. Mambrini, G.; Mandolini, M.; Rossi, L.; Pierige, F.; Capogrossi, G.; Salvati, P.; Serafini, S.; Benatti, L.; Magnani, M., Ex vivo encapsulation of dexamethasone sodium phosphate into human autologous erythrocytes using fully automated biomedical equipment. *Int. J. Pharmaceut.* **2017,** *517* (1-2), 175-184.

31. van Zwieten, R.; Bochem, A. E.; Hilarius, P. M.; van Bruggen, R.; Bergkamp, F.; Hovingh, G. K.; Verhoeven, A. J., The cholesterol content of the erythrocyte membrane is

an important determinant of phosphatidylserine exposure. *Biochim. Biophys. Acta, Mol. Cell Biol. Lipids* **2012,** *1821* (12), 1493-1500.

32. Zidovetzki, R.; Levitan, I., Use of cyclodextrins to manipulate plasma membrane cholesterol content: Evidence, misconceptions and control strategies. *Biochim. Biophys. Acta, Biomembr.* **2007,** *1768* (6), 1311-1324.

33. van Meer, G.; Voelker, D. R.; Feigenson, G. W., Membrane lipids: where they are and how they behave. *Nat. Rev. Mol. Cell Biol.* **2008,** *9* (2), 112-124.

34. Kessel, A.; Ben-Tal, N.; May, S., Interactions of cholesterol with lipid bilayers: The preferred configuration and fluctuations. *Biophys. J.* **2001,** *81* (2), 643-658.

35. Cooper, R. A., Influence of increased membrane cholesterol on membrane fluidity and cell-function in human red blood-cells. *J. Supramol. Struct.* **1978,** *8* (4), 413-430.

36. Yang, S. T.; Kreutzberger, A. J. B.; Lee, J.; Kiessling, V.; Tamm, L. K., The role of cholesterol in membrane fusion. *Chem. Phys. Lipids* **2016,** *199*, 136-143.

37. Chabanel, A.; Flamm, M.; Sung, K. L.; Lee, M. M.; Schachter, D.; Chien, S., Influence of cholesterol content on red cell membrane viscoelasticity and fluidity. *Biophys. J.* **1983,** *44* (2), 171-6.

38. Meleard, P.; Gerbeaud, C.; Pott, T.; FernandezPuente, L.; Bivas, I.; Mitov, M. D.; Dufourcq, J.; Bothorel, P., Bending elasticities of model membranes: Influences of temperature and sterol content. *Biophys. J.* **1997,** *72* (6), 2616-2629.

39. Jemaa, M.; Fezai, M.; Bissinger, R.; Lang, F., Methods employed in cytofluorometric assessment of eryptosis, the suicidal erythrocyte death. *Cell Physiol. Biochem.* **2017,** *43* (2), 431-444.

40. Schneider, C. A.; Rasband, W. S.; Eliceiri, K. W., NIH Image to ImageJ: 25 years of image analysis. *Nat. Methods* **2012,** *9* (7), 671-675.

41. Sarshar, M.; Lu, T.; Anvari, B., Combined optical micromanipulation and interferometric topography (COMMIT). *Biomed. Opt. Express* **2016,** *7* (4), 1365-1374.

42. Wang, Z.; Millet, L.; Mir, M.; Ding, H. F.; Unarunotai, S.; Rogers, J.; Gillette, M. U.; Popescu, G., Spatial light interference microscopy (SLIM). *Opt. Express* **2011,** *19* (2), 1016-1026.